A Description of the GFDL Global Spectral Model

CHARLES T. GORDON AND WILLIAM F. STERN

Geophysical Fluid Dynamics Laboratory/NOAA, Princeton University, Princeton, NJ 08540

(Manuscript received 8 May 1981, in final form 16 March 1982)

ABSTRACT

A multi-level, global, spectral transform model of the atmosphere, based upon spherical harmonics, has been developed at GFDL. The basic model has nine sigma levels in the vertical and rhomboidal spectral truncation at wavenumber 30. However, finer spectral or vertical resolution versions are available as well. The model's efficient semi-implicit time differencing scheme does not appear to adversely affect medium range predictions. The model has physical processes commonly associated with grid point GCM's. Two unique features are a linearized virtual temperature correction and an optional, spectrally-computed nonlinear horizontal diffusion scheme. A parameterization of vertical mixing based upon the turbulent closure method is also optional.

The GFDL spectral model has been widely utilized at GFDL for extended range weather prediction experiments. In addition, it has been adapted and applied to climate studies, four-dimensional data assimilation experiments and even to the atmosphere of Venus. These applications are briefly reviewed.

1. Introduction

Models used for numerical weather prediction or climate simulation must often meet rather stringent computational efficiency as well as accuracy requirements. For many applications, global/hemispheric spectral transform models can satisfy this pair of requirements. In such models, scalar variables are represented on the sphere by a truncated series of spherical harmonics. Finite differences are usually employed in the sigma-coordinate direction, although finite elements have been used by Staniforth and Daley (1977). In contrast, three-dimensional spectral representations, as in Machenhauer and Daley (1972), have not met with much success.

The spectral transform method, proposed by Orszag (1970) and refined by Eliasen *et al.* (1970), Orszag (1971) and Bourke (1972) is an essential element of the above models. This method is much more efficient than the "interaction coefficient" method at calculating nonlinear advection terms, as shown by Bourke (1972). Also, it has the versatility to compute grid point physical processes, which the "interaction coefficient" method lacks.

The relative merits of spectral transform models vs second-order accurate, energy conserving, nonstaggered grid point models of comparable overall accuracy are fairly well established (Daley *et al.*, 1976; Baede and Hansen, 1977). Spectral transform models have the following advantages: 1) Their more compact representation results in a significant reduction in computer memory; 2) they have competitive, if not somewhat improved computational efficiency at low to moderate horizontal resolution; 3) less effort is required to implement and less overhead to use efficient semi-implicit time differencing schemes; 4) there is no need for polar filtering; 5) the geopotential height gradient terms can be evaluated directly on sigma-coordinate surfaces without special treatment to insure computational stability; 6) phase lag errors of midlatitude synoptic disturbances are reduced noticeably (Daley *et al.*, 1976); and 7) the spectral representation and transformation algorithms can readily exploit the potential of so-called vector super-computers.

On the other hand, spectral models have some disadvantages: 1) They may resolve smaller scale features such as midlatitude fronts less sharply than grid point models (Simmons and Hoskins, 1975); 2) the truncated spectral representation of water vapor is not positive definite and a more elaborate negative borrowing scheme is required for extended integrations (see Section 6); 3) spherical harmonics are not suitable for limited domains, except for applications where a sector with periodic boundary conditions is justified; and 4) the number of arithmetic operations increases faster in spectral transform models than in finite difference models as the horizontal resolution is refined.

Several spectral models suitable for short and/or medium range weather prediction have already been described in various degrees of detail including: the Australian National Meteorological Research Centre (ANMRC) model (Bourke, 1974); a preliminary Geophysical Fluid Dynamics Laboratory (GFDL) spectral model developed by Gordon and Stern

(1974); the Canadian Meteorological Centre model (Daley *et al.*, 1976); the European Centre for Medium Range Weather Forecasts (ECMWF) model (Baede and Hansen, 1977) based upon the Hoskins and Simmons (1975) Reading University model; the National Meteorological Center model (Sela, 1980); and the Naval Post Graduate School model (Lubeck *et al.*, 1977). In addition, Bourke *et al.* (1977), Manabe *et al.* (1979), and Boer and McFarlane (1978) have constructed low to moderate resolution spectral models for carrying out climate simulation and related studies.

The GFDL global spectral model was developed in response to a suggestion by Machenhauer and Robert to Miyakoda in 1971. Bourke's (1972) formulation of the spectral transform method was adopted due to its simplicity. The computer code for Bourke's (1972) *barotropic* spectral model was kindly provided to us during the initial stage of model development. Thus, the spectral aspects of the Bourke (1974) and GFDL spectral models are very similar. However, we emphasize that the GFDL multilevel spectral prediction model including the physical processes and semi-implicit time differencing scheme has been developed independently.

Since 1974, extensive improvements have been made to the GFDL spectral prediction model, transforming it into a respectable extended range prediction model. For example, the rhomboidal spectral resolution has been increased from 15 to 30 waves and many more physical processes have been incorporated. The latter are essentially of the type found in grid point general circulation models (GCM's) at GFDL. A variety of options, including finer spectral or vertical resolution and more advanced parameterizations of physical processes are available as well.

Two apparently unique features of the GFDL spectral model are a linearized virtual temperature correction and an optional, spectrally-computed nonlinear horizontal diffusion scheme. The Mellor-Yamada (1974) turbulent closure parameterization of turbulent vertical mixing which was previously incorporated into the GFDL grid point prediction model by Miyakoda and Sirutis (1977), is a particularly promising option.

Since 1974, the GFDL spectral prediction model has been adapted and applied, within GFDL, to a wide range of research activities. These include extended and long range prediction experiments, four-dimensional assimilation of atmospheric data, climate simulation and sensitivity studies, and simulation of the Venusian atmosphere. Without the development of the GFDL spectral model, these activities would have been delayed considerably and the four-dimensional assimilation of FGGE data may not have been attempted by GFDL.

For the above reasons, a more definitive and accessible documentation of the present GFDL spectral model than that given by Gordon and Stern (1974) would be useful. This will be the primary objective of the present paper. In addition, a brief review of the applications of spectral models at GFDL will be given.

The partial differential equations and auxiliary equations that govern the model are specified in Section 2. The notation for finite differences in the vertical is introduced in Section 3, and the governing equations are developed somewhat further. The discussions in Section 4 and Section 5 focus on the model's spectral aspects and semi-implicit time differencing scheme. Any overlap here with derivations by previous authors, notably Bourke (1974), is for the sake of completeness. The model's grid point physical processes and orography are treated in Sections 6 and 7, while its computational efficiency is discussed in Section 8. The applications of the spectral model at GFDL are briefly reviewed in Section 9. Finally, concluding remarks are given in Section 10.

2. The governing equations

The equations are formulated for a thin spherical shell, using σ as the vertical coordinate. The prognostic equations consist of the equations of motion in vector form

$$\partial \mathbf{V}/\partial t = -(\zeta + f)\hat{k} \times \mathbf{V} - \nabla(\mathbf{V}\cdot\mathbf{V}/2) - \dot{\sigma}\partial\mathbf{V}/\partial\sigma - \nabla\Phi - RT_v\nabla q + \mathbf{F}_v, \quad (1)$$

the thermodynamics equation

$$\partial T/\partial t = -\mathbf{V}\cdot\nabla T' - \dot{\sigma}\partial T/\partial\sigma + \frac{RT}{C_p}\frac{\omega}{p} + F_T + \frac{Q_{\text{Rad}}}{C_p} + \frac{Q_c}{C_p}, \quad (2)$$

the water vapor equation

$$\partial r/\partial t = -\mathbf{V}\cdot\nabla r - \dot{\sigma}\partial r/\partial\sigma + F_r + C, \quad (3)$$

and the surface pressure equation

$$\partial q/\partial t = -\tilde{\mathbf{V}}\cdot\nabla q - \nabla\cdot\tilde{\mathbf{V}}. \quad (4)$$

The auxilliary diagnostic equations include the hydrostatic relation

$$\frac{\partial\Phi}{\partial \ln\sigma} = -RT_v, \quad (5)$$

the virtual temperature relation

$$T_v = T + 0.61\bar{T}r, \quad (6)$$

an expression for the vertical pressure velocity, i.e.,

$$\omega = p\left[\frac{\dot{\sigma}}{\sigma} + (\mathbf{V} - \tilde{\mathbf{V}})\cdot\nabla q - \nabla\cdot\tilde{\mathbf{V}}\right], \quad (7)$$

and the continuity equation

$$\dot{\sigma} = -\int_0^\sigma (\nabla\cdot\mathbf{V} - \nabla\cdot\tilde{\mathbf{V}})d\sigma - \int_0^\sigma (\mathbf{V} - \tilde{\mathbf{V}})\cdot\nabla q d\sigma. \quad (8)$$

Above, $(\tilde{\ })$ denotes the vertical averaging operator $\int_0^1(\ )d\sigma$. Also, V is the horizontal wind vector with components u and v, T the temperature, r the water vapor mixing ratio, q the natural logarithm of the surface pressure p_s, Φ the geopotential, T_v the virtual temperature, σ the vertical coordinate ($\sigma = p/p_s$, where p is the pressure), ω the vertical pressure velocity, $\dot{\sigma}$ the vertical sigma velocity, t the time; ∇ the horizontal gradient operator, λ, φ the longitude and latitude, ζ the vertical component of relative vorticity, D the horizontal divergence, f the Coriolis parameter, $\hat{k}$ is a unit vector normal to the sphere, R is the gas constant, C_p the specific heat capacity at constant pressure, $\bar{T}$ is a reference temperature and $\bar{T}_v$ is a reference virtual temperature which depend only on σ, $T' = T - \bar{T}$ and $T'_v = T_v - \bar{T}_v$, Q_{Rad} is the rate of radiative heating, Q_c the rate of condensational heating, C the rate of condensation of water vapor, and $\mathbf{F}_V$, F_T and F_r represent the diffusion of momentum, temperature and water vapor, respectively.

Eqs. (1)–(8) are rather standard, except perhaps for the virtual temperature relation. In principle, its inclusion makes the model more realistic. The virtual temperature directly affects only the hydrostatic equation and the geopotential gradient terms in the equation of motion, just as in Miyakoda (1973). However, Miyakoda's formula for T_v, i.e., $T(1 + 1.61r)/(1 + r)$ has been simplified to an expression that is linear with respect to T and r. Since $r \ll 1$ and $(T - \bar{T})/T \leqslant 0.2$, our linearized virtual temperature correction ($T_v - T = 0.61\bar{T}r$) should generally agree with Miyakoda's to within 20%. The linearized form is computationally more efficient, requires less computer memory and is more convenient if semi-implicit time differencing is applied.

3. The vertical representation

The notation Z_k indicates that the arbitrary variable Z is evaluated at the full sigma level σ_k, $k = 1, 2, \cdots kx$. Similarly, $Z_{k+1/2}$ is evaluated at the half level $\sigma_{k+1/2}$. If the variable in question, e.g., T_v, already has a subscript, then the alternate notation $T_v(k)$ is used.

The full and half sigma levels are the same as in the nine-level GFDL grid point model (see Table 1). The variables u, v, T, T_v and r as well as ζ, D and Φ are evaluated at the full levels σ_k, $k = 1, 2, \cdots kx$. In contrast, $\dot{\sigma}$ and ω are evaluated at the half levels $\sigma_{k+1/2}$, $k = 1, 2, \cdots kx - 1$. At the top boundary ($\sigma_{1/2} = 0$) and at the bottom boundary ($\sigma_{kx+1/2} = 1$), $\dot{\sigma} = 0$. Variables at adjacent half levels are linearly averaged to obtain estimates at full levels and vice versa. For example,

$$\dot{\sigma}_k = (\dot{\sigma}_{k+1/2} + \dot{\sigma}_{k-1/2})/2.$$

Similarly,

$$Z_{k+1/2} = (Z_k + Z_{k+1})/2,$$

where Z represents $u\cos\varphi$, $v\cos\varphi$, T, r, etc.

The vertical advection term $\dot{\sigma}\partial Z/\partial\sigma$ at level k is approximated by the second-order accurate finite difference operator $W_k(\dot{\sigma}, Z)$, where

$$W_k(\dot{\sigma}, Z) = \frac{1}{2}\left[\dot{\sigma}_{k+1/2}\frac{Z_{k+1} - Z_k}{(\Delta\sigma)_{k+1/2}} + \dot{\sigma}_{k-1/2}\frac{Z_k - Z_{k-1}}{(\Delta\sigma)_{k-1/2}}\right] \quad (9)$$

and $(\Delta\sigma)_{k+1/2} = \sigma_{k+1} - \sigma_k$. The values of Z at $k = 0$ and at $k = kx + 1$ are not needed since $\dot{\sigma}_{1/2} = 0$ and $\dot{\sigma}_{kx+1/2} = 0$.

The vertical average finite difference operator applied to the divergence D is

$$\tilde{D} = \sum_{k=1}^{kx} D_k(\Delta\sigma)_k. \quad (10)$$

This operator is applied to V $\cos\varphi$ as well.

The variable $\dot{\sigma}$ is conveniently expressed as the sum of $\dot{\sigma}_L + \dot{\sigma}_N$, where $\dot{\sigma}_L$ is linear with respect to the divergence and $\dot{\sigma}_N$ is a nonlinear function of V $\cos\varphi$ and q. The finite difference formulas

$$\dot{\sigma}_L(k + \tfrac{1}{2}) = \sum_{k'=1}^{k}(\tilde{D} - D_{k'})(\Delta\sigma)_{k'} \quad (11)$$

and

$$\dot{\sigma}_N(k + \tfrac{1}{2}) = -\frac{1}{\cos^2\varphi}\left\{\sum_{k'=1}^{k}[(\mathbf{V}\cos\varphi)_{k'} - \tilde{\mathbf{V}}\cos\varphi]\cdot\cos\varphi\nabla q(\Delta\sigma)_{k'}\right\}, \quad (12)$$

at levels $k = 1, \cdots, kx - 1$, correspond to the first and second integrals on the right-hand side of Eq. (8). Also, $\dot{\sigma}_L$ and $\dot{\sigma}_N$ are set equal to zero at the top

TABLE 1. The GFDL σ levels and half levels for the nine-level model

k	0	1	2	3	4	5	6	7	8	9
σ_k	—	0.0089	0.074	0.189	0.336	0.500	0.664	0.811	0.926	0.991
$\sigma_{k+1/2}$	0.0	0.0343	0.126	0.259	0.417	0.583	0.741	0.874	0.966	1.000

and bottom boundaries. The linear averaging procedure is applied to Eqs. (11) and (12) to calculate $\dot{\sigma}_L(k)$ and $\dot{\sigma}_N(k)$.

The prognostic equations and hydrostatic relation are now rewritten incorporating the vertical finite difference notation and the finite difference operator W_k. Their form has been modified somewhat in order to apply Bourke's (1972) efficient spectral transform method. For the same reason, the vorticity ζ and divergence D ultimately replace the wind components u and v as prognostic variables. Therefore a vorticity equation and a divergence equation are needed. They are easily derived if we first introduce the vector

$$\mathbf{S}_k = -(\zeta_k + f)\hat{k} \times (\mathbf{V}\cos\varphi)_k - W_k(\dot{\sigma}, \mathbf{V}\cos\varphi) - RT'_v(k)\cos\varphi\nabla q + \mathbf{F}_{VN}(k)\cos\varphi, \quad (13)$$

with components S^{λ}_k and S^{φ}_k, and the kinetic energy density

$$E_k = \frac{(u\cos\varphi)_k^2 + (v\cos\varphi)_k^2}{\cos^2\varphi}. \quad (14)$$

Substitution of $\mathbf{S}_k$ and E_k into the equations of motion, i.e., Eq. (1) at levels $k = 1, 2, \cdots kx$, yields the equation

$$\frac{\partial \mathbf{V}_k}{\partial t} = \frac{\mathbf{S}_k}{\cos\varphi} - \nabla E_k - \nabla(\Phi + R\bar{T}_v q)_k + \mathbf{F}_{VL}(k). \quad (15)$$

Above, $\mathbf{F}_{VL}$ and $\mathbf{F}_{VN}$ represent the linear and nonlinear contributions to $\mathbf{F}_V$. Similarly, F_T and F_r will be decomposed later into linear contributions F_{TL} and F_{rL} and nonlinear components F_{TN} and F_{rN}. In Eq. (15), $\bar{T}_v(k) = \bar{T}_k(1 + 0.61\bar{r}_k)$, where $\bar{r}_k$ is a reference mixing ratio. After applying the $\hat{k}\cdot\nabla\times$ and $\nabla\cdot$ linear differential operators to Eq. (15), we obtain the vorticity equation

$$\partial\zeta_k/\partial t = -\nabla\cdot\left(\hat{k}\times\frac{\mathbf{S}_k}{\cos\varphi}\right) + \hat{k}\cdot\nabla\times\mathbf{F}_{VL}(k) \quad (16)$$

and the divergence equation

$$\partial D_k/\partial t = \nabla\cdot\left(\frac{\mathbf{S}_k}{\cos\varphi}\right) - \nabla^2 E_k - \nabla^2(\Phi + R\bar{T}_v q)_k + \nabla\cdot\mathbf{F}_{VL}(k). \quad (17)$$

These equations contain essentially the same information as Eq. (15) since no terms have been discarded. Yet their form is simple, since the equations of motion [Eq. (1)] have not been differentiated term by term. The equations of motion are still used in the sense that $\mathbf{S}_k$ and E_k are calculated from Eq. (13) and Eq. (14) as an intermediate step. The latter terms are closely related to the nonlinear terms $\mathbf{S}_k/\cos\varphi$ and ∇E_k of Eq. (15).

Next, the form of the thermodynamic equation (2) is modified. First, using Eq. (7), ω is expressed as a function of $\dot{\sigma}$, $\tilde{D}$ and nonlinear terms in Eq. (2). Secondly, since $\dot{\sigma} = \dot{\sigma}_L + \dot{\sigma}_N$ and $T = \bar{T} + T'$, the quadratic form $T\dot{\sigma}$ may be set equal to $\bar{T}\dot{\sigma}_L + (\bar{T}\dot{\sigma}_N + T'\dot{\sigma})$ in Eq. (2). Thirdly, the horizontal thermal advection term is differentiated by parts, i.e., $-\mathbf{V}\cdot\nabla T'$ is written as $-\nabla\cdot T'\mathbf{V} + T'D$. At this point, nonlinear and linear terms on the right-hand side of Eq. (2) are regrouped separately. The nonlinear terms are consolidated into $\Theta_N(k) - \nabla\cdot T'_k\mathbf{V}_k$, where

$$\Theta_N(k) = T'_k D_k - [W_k(\dot{\sigma}_N\bar{T}) + W_k(\dot{\sigma}, T')] + \frac{R}{C_p}\left[\bar{T}_k\frac{\dot{\sigma}_N(k)}{\sigma_k} + T'_k\left(\frac{\dot{\sigma}_k}{\sigma_k} - \tilde{D}\right)\right] + \frac{R}{C_p}T_k\frac{[(\mathbf{V}\cos\varphi)_k - \tilde{\mathbf{V}}\cos\varphi]\cdot\cos\varphi\nabla q}{\cos^2\varphi} + \frac{Q_{\text{Rad}}}{C_p}(k) + F_{TN}(k). \quad (18)$$

The terms which are linear with respect to $\dot{\sigma}_L$ and D can be expressed as $-[W_k(\dot{\sigma}_L, \bar{T}) - R\bar{T}_k/C_p(\dot{\sigma}_L(k)/\sigma_k - \tilde{D})]$, or equivalently as the product of a matrix $\underset{\sim}{\Lambda}$ and a column vector $\mathbf{D}$ of divergences $\mathbf{D}_k$, $k = 1, \cdots, kx$. In other words,

$$\sum_{k'=1}^{kx}\Lambda_{k,k'}D_{k'} = -\left[W_k(\dot{\sigma}_L, \bar{T}) - \frac{R\bar{T}_k}{C_p}\left(\frac{\dot{\sigma}_L(k)}{\sigma_k} - \tilde{D}\right)\right]. \quad (19)$$

To derive an explicit formula for the matrix elements $\Lambda_{k,k'}$, the operator W_k and variables $\tilde{D}$ and $\dot{\sigma}_L$ are eliminated using Eqs. (9), (10) and (11), respectively and $\sum_{k'=1}^{k-1}(\Delta\sigma)_{k'}$ is set equal to $\sigma_{k-1/2}$. After lengthy manipulations, we obtain

$$\Lambda_{k,k'} = \begin{cases} (\tilde{a}_k - \tilde{d}_k)(\Delta\sigma)_{k'}, & k' < k \\ (\tilde{b}_k - \tilde{d}_k)(\Delta\sigma)_{k'}, & k' = k \\ -\tilde{d}_k(\Delta\sigma)_{k'}, & k' > k \end{cases}, \quad (20)$$

where

$$\tilde{a}_k = \frac{(1-\delta_{k,kx})}{2}\left[\frac{\bar{T}_{k+1} - \bar{T}_k}{(\Delta\sigma)_{k+1/2}} - \frac{R\bar{T}_k}{C_p\sigma_k}\right] + \frac{(1-\delta_{k,1})}{2}\left[\frac{\bar{T}_k - \bar{T}_{k-1}}{(\Delta\sigma)_{k-1/2}} - \frac{R\bar{T}_k}{C_p\sigma_k}\right], \quad (21a)$$

$$\tilde{b}_k = \frac{(1-\delta_{k,kx})}{2}\left[\frac{(\bar{T}_{k+1} - \bar{T}_k)}{(\Delta\sigma)_{k+1/2}} - \frac{R\bar{T}_k}{C_p\sigma_k}\right], \quad (21b)$$

$$\tilde{d}_k = \tilde{a}_k\sigma_{k-1/2} + \tilde{b}_k(\Delta\sigma)_k + \frac{R\bar{T}_k}{C_p} \quad (21c)$$

and δ is the Kronecker delta function. The matrix $\underset{\sim}{\Lambda}$ is generally nonsymmetric.

Substitution of Eqs. (18) and (19) into Eq. (2) yields the thermodynamic equation

$$\partial T_k/\partial t = \Theta_N(k) - \nabla \cdot T_k' \mathbf{V}_k + \sum_{k'=1}^{kx} \Lambda_{k,k'} D_{k'} + F_{TL}(k). \quad (22)$$

Differentiating the horizontal advection terms by parts in Eq. (3), we obtain the water vapor equation

$$\partial r_k/\partial t = \mu_k - \nabla \cdot r_k \mathbf{V}_k + F_{rL}(k). \quad (23)$$

Most of the nonlinear terms have been consolidated into

$$\mu_k = r_k D_k - W_k(\dot{\sigma}, r) + F_{rN}(k). \quad (24)$$

Also, the surface pressure equation is rewritten as

$$\partial q/\partial t = M - \tilde{D}, \quad (25)$$

where

$$M = -\frac{(\tilde{\mathbf{V}} \cos\varphi) \cdot (\cos\varphi \nabla q)}{\cos^2\varphi}. \quad (26)$$

Condensation induces changes in T_k and r_k which are calculated after Eqs. (22) and (23) have been solved, using a convective adjustment large-scale condensation scheme (see Sections 4c and 6f). Therefore, Q_c and C do not appear in Eqs. (22) and (23).

The hydrostatic Eq. (5) is integrated upwards from the surface. The half layer between σ_{kx} and $\sigma_{kx+1/2}$ is treated specially to obtain Φ_{kx}. The relevant finite difference approximations to Eq. (5) are

$$\Phi_{kx} = \Phi_s + \hat{\alpha} T_v(kx) + \hat{\beta} T_v(kx - 1) \quad (27a)$$

and

$$\Phi_k = \Phi_{k+1} + \alpha_k T_v(k) + \beta_k T_v(k + 1), \quad (27b)$$

for

$$k = kx - 1, kx - 2, \cdots, 1,$$

where Φ_s is the geopotential evaluated at the surface. The weights α_k and β_k are chosen such that the mean virtual temperature of the interior layer between σ_k and σ_{k+1} is $\frac{1}{2}[T_v(k) + T_v(k + 1)]$. Consequently, for $k < kx$

$$\alpha_k = \frac{R}{2} \ln(\sigma_{k+1}/\sigma_k), \quad (28a)$$

$$\beta_k = \frac{R}{2} \ln(\sigma_{k+1}/\sigma_k). \quad (28b)$$

Similarly, the mean virtual temperature of the half layer between σ_{kx} and $\sigma_{kx+1/2}$ is $\frac{1}{2}[T_v(kx) + T_v(kx + \frac{1}{2})]$. However, $T_v(kx + \frac{1}{2})$ is itself extrapolated in $\ln\sigma$ space from $T_v(kx)$ and $T_v(kx - 1)$. Therefore the coefficients

$$\hat{\alpha} = \frac{R}{2} \ln\left[\frac{\sigma_{kx+(1/2)}}{\sigma_{kx}}\right] \left\{ 2 + \frac{\ln\left[\frac{\sigma_{kx+(1/2)}}{\sigma_{kx}}\right]}{\ln\left(\frac{\sigma_{kx}}{\sigma_{kx-1}}\right)} \right\} \quad (29a)$$

and

$$\hat{\beta} = -\frac{R}{2} \ln\left[\frac{\sigma_{kx+(1/2)}}{\sigma_{kx}}\right] \left\{ \frac{\ln\left[\frac{\sigma_{kx+(1/2)}}{\sigma_{kx}}\right]}{\ln\left(\frac{\sigma_{kx}}{\sigma_{kx-1}}\right)} \right\}, \quad (29b)$$

are more complicated than α_k and β_k.

4. Development of the spectral equations

The essential spectral aspects of the GFDL spectral model are the spherical harmonics representation, the transformation of the equations to the spectral domain, and the computation of nonlinear terms by the spectral-grid transform method.

a. The spectral representation

The scalar variables ζ, D, T, r, q, and Φ as well as $u\cos\varphi$, $v\cos\varphi$ and $\cos\varphi\nabla q$ are expanded in series of spherical harmonics. The arbitrary variable Z has the expansion

$$Z = \sum_{m=-M}^{M} \sum_{n=|m|}^{|m|+\hat{J}} Z_n^m Y_n^m, \quad (30)$$

where the time-dependent spectral coefficients Z_n^m are complex. The notation $Z_n^m(k)$ will indicate that Z_n^m is evaluated at sigma level k. The reference to k may be suppressed, if no ambiguity arises. The ordinary spherical harmonic Y_n^m is a function of λ and φ. Furthermore, $Y_n^m = P_n^m(\sin\varphi)e^{im\lambda}$, where P_n^m is an associated Legendre polynomial of degree n and zonal wavenumber (rank) m. The P_n^m are normalized, i.e.,

$$\int_{-\pi/2}^{\pi/2} P_n^m P_{n'}^m \cos\varphi d\varphi = \delta_{nn'}$$

and

$$P_n^{-m} = (-1)^m P_n^m.$$

In Eq. (30), $\hat{J} = J + 1$ for $u\cos\varphi$, $v\cos\varphi$ and $\cos\varphi\partial q/\partial\varphi$, and $\hat{J} = J$ for the other variables. The effective meridional wave number is $n - |m|$.

The basic GFDL spectral model version is called R30L09. Here, R30 denotes rhomboidal truncation at wavenumber 30, i.e., $M = J = 30$, while L09 indicates that the model has nine sigma levels. If triangular truncation were imposed, the integer n would lie within the range $|m| \leq n \leq M$. For example, a T40L15 spectral model would denote triangular truncation at zonal wavenumber $M = 40$ and 15 sigma levels. Rhomboidal truncation was chosen over triangular primarily for its greater potential for vectorization on the Texas Instruments Advanced Scientific Computer (the ASC). In principle, the parameters M and J and hence the spectral resolution are easily varied. Of course, the maximum resolution

is constrained by core and cpu time limitations. The ASC computer can accommodate an R45L09 or R30L18 global spectral model or an R72L09 hemispheric model. The resolution characteristics of the various models are summarized in Table 2.

Since $\mathbf{V} = k \times \nabla\psi + \nabla\chi$, $\zeta = \nabla^2\psi$ and $D = \nabla^2\chi$ (where ψ is the streamfunction, χ the velocity potential and ∇^2 the Laplacian on the sphere), the spectral coefficients of $u\cos\varphi$ and $v\cos\varphi$ may be computed from the spectral coefficients of ζ and D. Following Bourke (1972),

$$\begin{pmatrix} U_n^m \\ V_n^m \end{pmatrix} = -\frac{a^2}{n(n+1)}\left[(n-1)\epsilon_n^m \begin{pmatrix} \zeta_{n-1}^m \\ D_{n-1}^m \end{pmatrix} + (n+2)\epsilon_{n+1}^m \begin{pmatrix} \zeta_{n+1}^m \\ D_{n+1}^m \end{pmatrix} + im\begin{pmatrix} D_n^m \\ \zeta_n^m \end{pmatrix}\right], \quad (31)$$

where

$$\epsilon_n^m = \left(\frac{n^2 - m^2}{4n^2 - 1}\right)^{1/2}.$$

By convention, $\zeta_{-1}^m = 0$ and $D_{-1}^m = 0$.

b. Transformation of the equations to the spectral domain

Consider the partial differential equation $\partial Z/\partial t = L + N$. Here, Z is a prognostic variable ($\partial Z/\partial t = 0$ if the equation is diagnostic), whose spectral coefficients Z_n^m are known at time t. The linear terms are each evaluated in the spectral domain and L denotes their sum. Linear differential operators present no difficulty since $\partial Y_n^m/\partial\lambda = imY_n^m$ while $\cos\varphi\partial Y_n^m/\partial\varphi$ projects onto Y_{n+1}^m and Y_{n-1}^m. The nonlinear terms, whose sum is denoted by N, are evaluated by the transform method (see Section 4c). Substituting the spectral expansions of Z, L and N into the above partial differential equation, multiplying by the complex conjugate $(Y_n^m)^*$, integrating over the globe, and applying the orthogonality relation

$$\frac{1}{2\pi}\int_0^{2\pi}\int_{-\pi/2}^{\pi/2} Y_{n'}^{m'}(Y_n^m)^* \cos\varphi d\varphi d\lambda = \delta_{nn'}\delta_{mm'},$$

yields the ordinary differential equation $dZ_n^m/dt = L_n^m + N_n^m$ for the time-varying spectral coefficients Z_n^m.

c. Transform method

Bourke's (1972, 1974) transform method is used instead of the interaction coefficient method to evaluate nonlinear dynamics terms and grid point physical processes. Its main virtues are computational efficiency and compatibility with existing formulations of physical processes. The transform method is subdivided into three steps:

STEP 1

The spectral coefficients for $\zeta_k + f$, D_k, $(u\cos\varphi)_k$, $(v\cos\varphi)_k$, r_k, q and $\cos\varphi\nabla q$ are transformed to a

TABLE 2. Resolution characteristics of the GFDL spectral models and N48 grid point model.

Model	Domain[a]	Number of spectral degrees of freedom[b]	$N_\lambda/\Delta\lambda$[c]	$N_\varphi/\Delta\varphi$[d]	Application
R15	G, H	496	48/8.0°	40/4.8°	Mainly for checkout, climate studies, simulation of Venusian atmosphere.
R21	G, H	946	64/5.7°	54/3.4°	For checkout, experimental prediction studies, climate studies.
R30	G, H	1891	96/4.0°	80/2.4°	Extensive use for extended and long range experimental prediction studies, climate studies; 4-dimensional analysis.
T42	H	1849	128/2.9°	64/2.9°	Very limited use for extended range experimental prediction studies.
R42	G, H	3655	128/2.9°	106/1.7°	
R45	G	4186	138/2.7°	114/1.6°	
R60	H	7381	184/2.0°	152/1.2°	
N48[e]	G	—	192/1.9° (tropics) decreasing to 36/10° (polar)	96/1.9°	For extended range and long-range experimental prediction studies.

[a] G = global, H = hemispheric.
[b] Number of spectral degrees of freedom = $(2M + 1)(M + 1)$ for rhomboidal, $(M + 1)^2$ for triangular *global* spectral models.
[c] N_λ = number of longitudes. Δ_λ = approximate nominal longitudinal increment of transform grid = $3M$ for spectral models or longitudinal increment of the modified Kurihara grid.
[d] N_φ = number of (Gaussian) latitudes. Δ_φ = approximate nominal latitudinal increment of transform grid = $5M/2$ for rhomboidal or $3M/2$ for triangular global spectral models or latitudinal increment of the modified Kurihara grid.
[e] N48 denotes the number of grid points between pole and equator.

Gaussian latitude–longitude grid with K latitudes and L equi-spaced longitudes. The numerical values of K and L depend upon the model's resolution. The transformation is carried out in two stages. First, a Legendre transform is evaluated for each spectral variable at Gaussian latitude φ_j, i.e., the latitude corresponding to the jth root of the associated Legendre polynomial P_k^0. For a particular variable Z, the Legendre transform has the form

$$Z_n^m \rightarrow Z_{(m)}(\varphi_j; t) = \sum_{n=|m|}^{|m|+\hat{J}} Z_n^m P_n^m. \quad (32a)$$

The resulting Fourier harmonics $Z_{(m)}$ are then Fourier-transformed to longitudes $\lambda_l = 2\pi l/L$, $1 < l < L$. Symbolically,

$$Z_{(m)} \rightarrow Z(\lambda_l, \varphi_j; t) = \sum_{m=-M}^{M} Z_{(m)} e^{im\lambda_l}. \quad (32b)$$

Note that the Legendre transforms are evaluated only once per latitude. This helps render the process efficient. As a rule, fast Fourier transform (FFT) algorithms should accelerate the calculation of Eq. (32b). But on the ASC computer, the ordinary transform was computationally more efficient than the currently available FFT algorithms for $L < 256$ points. The inability of the latter to fully vectorize on this vector supercomputer apparently more than compensates for their intrinsic efficiency.

STEP 2

Nonlinear dynamics and physical process terms of each prognostic equation can now be calculated at the equi-spaced grid points along latitude circle φ_j. The variables transformed in step 1 provide the necessary information to compute $\dot{\sigma}_k$, $\dot{\sigma}_{k+1/2}$, $\dot{\sigma}_N(k)$, $\dot{\sigma}_N(k + \frac{1}{2})$, $W_k(\dot{\sigma}, \mathbf{V}\cos\varphi)$, $W_k(\dot{\sigma}_N, T)$, $W_k(\dot{\sigma}, T')$, $W_k(\dot{\sigma}, r)$, $T'_k\mathbf{V}_k$ and $r_k\mathbf{V}_k$, and ultimately $\mathbf{S}_k$, E_k, $\Theta_N(k)$, μ_k and M at latitude φ_j and longitudes $\lambda_l = 2\pi l/L$, $l = 1, 2, \cdots L$. The evaluation of the auxiliary nonlinear variables $\mathbf{S}$, Θ_N, μ and M reduces the number of transformations back to the spectral domain.

STEP 3

The appropriate nonlinear terms in Eqs. (16), (17), (22), (23) and (25) are transformed back to the spectral domain in two stages. First, Fourier transforms of E_k, $\Theta_N(k)$, μ_k and M, as well as $\partial S_k^\varphi/\partial\lambda$ and S_k^λ, $\partial S_k^\lambda/\partial\lambda$ and S_k^φ, $\partial T'_k(u\cos\varphi)_k/\partial\lambda$ and $T'_k(v\cos\varphi)_k$, and $\partial r'_k(u\cos\varphi)_k/\partial\lambda$ and $r'_k(v\cos\varphi)_k$ are computed at latitude φ_j. The latter four pairs of terms are needed to obtain divergences. During the second stage, inverse Legendre transformations are built up one latitude at a time using Gaussian quadrature. The procedure is most straightforward for the scalars E_k, $\Theta_N(k)$, μ_k and M. Denoting the Fourier transform of any of these by $Z_{(m)}(\varphi_j)$, the Gaussian quadrature formula is

$$Z_n^m = \sum_{j=1}^{K} w_{jK}(\varphi_j) Z_{(m)}(\varphi_j) P_n^m(\sin\varphi_j). \quad (33)$$

Here, the jth of K Gaussian weights w_{jk} is the effective area weight at latitude φ_j and K is the total number of Gaussian latitudes. Gaussian quadrature preserves the orthogonality relations for associated Legendre polynomials, i.e., $\sum_{j=1}^{K} w_{jk} P_n^m P_{n'}^m = \delta_{n,n'}$. According to Elsaesser (1966), the Gaussian weights were actually proposed by Neumann in 1838. In any case, Elsaesser (1966) and Eliasen *et al.* (1970) were apparently the first to use the quadrature formula (33) to spectrally analyze meteorological data and to integrate a spectral model, respectively.

A more complicated formula is needed for the divergences. Denoting $-\hat{k} \times \mathbf{S}_k/\cos\varphi$, $\mathbf{S}_k/\cos\varphi$, $T'_k\mathbf{V}_k$ or $r_k\mathbf{V}_k$ by the vector $\mathbf{Z}$ (with components Z^λ and Z^φ)

$$\nabla\cdot\mathbf{Z} = \frac{1}{a\cos^2\varphi}\left[\frac{\partial}{\partial\lambda}(Z^\lambda\cos\varphi) + \cos\varphi\frac{\partial}{\partial\varphi}(Z^\varphi\cos\varphi)\right], \quad (34a)$$

in spherical coordinates. In analogy with Eq. (33), it might appear that the quadrature formula for $\nabla\cdot\mathbf{Z}$ should involve $(\partial Z^\varphi\cos\varphi/\partial\varphi)P_n^m$. But this expression is differentiated by parts since $\partial Z^\varphi\cos\varphi/\partial\varphi$ is not known at latitude φ_j whereas $Z^\varphi\cos\varphi$ and $\cos\varphi dP_n^m/d\varphi$ are. Therefore

$$(\nabla\cdot\mathbf{Z})_n^m = \frac{1}{a}\sum_{j=1}^{K}\frac{w_{jK}(\varphi)}{\cos^2\varphi}[im(Z^\lambda\cos\varphi)_{(m)}P_n^m - (Z^\varphi\cos\varphi)_{(m)}(\cos\varphi dP_n^m/d\varphi)]. \quad (34b)$$

Every factor in Eq. (34b) is evaluated at latitudes φ_j, $j = 1, 2, \cdots K$.

In the above manner, one obtains the spectral representation of the time rate of change due to nonlinear terms in Eqs. (16), (17), (22), (23) and (25). Given two arbitrary variables A and B, no aliasing of the elementary quadratic expressions $A\cdot B$, $\nabla A\cdot\nabla B$, or the Jacobian $J(A, B)$ occurs when evaluated by the spectral interaction coefficient method (Merilees, 1968). Furthermore, the horizontal advection terms can be decomposed into elementary quadratic expressions of the above forms. These properties are preserved in our rhomboidally truncated, spectral model, provided $K > J + (3/2)M$ and $L > 3M$. In practice, K and L are set equal to 80 and 96, respectively in the R30L09 model.

Convective adjustment/large scale condensation and nonlinear horizontal diffusion cause complications by requiring that a second set of transforma-

tions be carried out before those discussed above. The process is similar in that spectral arrays are transformed to the grid point domain one latitude at a time, calculations are made in the grid point domain, and the results are transformed back to the spectral domain. For example, spectral arrays for the unadjusted temperature T_u and unadjusted mixing ratio r_u are transformed to the grid point domain where the convective adjustment/large scale condensation algorithms of Manabe *et al.* (1965) are applied. Transforming the adjusted fields back to the spectral domain yields the desired variables T and r. But due to spectral truncation, adjustment in vertical columns is not necessarily preserved, when T and r are later transformed back to the grid point domain.

In parallel with the above computations, spectral variables such as ζ, D, $u\cos\varphi$, $v\cos\varphi$, T, r and q from the previous time step are transformed to the grid domain. Then deformation-related variables are calculated and transformed back to the spectral domain. These intermediate spectral variables are available for step 1 of the main body of transformations. Thus the nonlinear horizontal diffusion terms can be calculated in the grid point domain during step 2. More details are provided in Section 6.

d. The spectral equations

The prognostic vorticity Eq. (16), divergence Eq. (17), thermodynamics Eq. (22), water vapor Eq. (23) and surface pressure Eq. (25) as well as the hydrostatic equations (27a) and (27b) are readily transformed to the spectral domain by the above procedures. The form of the spectral equations is simplified if terms which are not linear with respect to D_k, Φ_k or q are added together to form the auxiliary variables

$$\xi_k = -\nabla\cdot\hat{k}\times\frac{\mathbf{S}_k}{\cos\varphi} + \hat{k}\cdot\nabla\times\mathbf{F}_{VL}(k), \quad (35)$$

$$\hat{\eta}_k = \nabla\cdot\frac{\mathbf{S}_k}{\cos\varphi} + \nabla\cdot\mathbf{F}_{VL}(k), \quad (36)$$

$$\Theta_k = \Theta_N(k) - \nabla\cdot T'_k\mathbf{V}_k + F_{TL}(k) \quad (37)$$

$$\Pi_k = \mu_k - \nabla\cdot r_k\mathbf{V}_k - F_{rL}(k), \quad (38)$$

in Eqs. (16), (17), (23) and (25), respectively. Note that $-\nabla^2E_k$ is not included in Eq. (36). In practice, E_k is transformed separately to the spectral domain. Since $(\nabla^2E)_n = -[n(n+1)/a^2]E_n^m$, the spectral coefficients $\hat{\eta}_n^m$ are replaced by

$$\eta_n^m(k) = \hat{\eta}_n^m(k) + \frac{n(n+1)}{a^2}E_n^m(k). \quad (39)$$

Incidentally, the linear diffusion terms are added to ξ_k, $\hat{\eta}_k$, Θ_k and Π_k in the spectral domain. Also, it is convenient to introduce the variable

$$\hat{P}_k = \Phi_k + R\bar{T}_v(k)q \quad (40)$$

into the spectral divergence Eq. (17). All terms that are linear with respect to $\hat{P}_k$ and D_k are now placed on the left-hand side of the prognostic equations. Finally, we obtain

$$\frac{d\zeta_n^m}{dt}(k) = \xi_n^m(k), \quad (41)$$

$$\frac{dD_n^m}{dt}(k) - \frac{n(n+1)}{a^2}\bar{\hat{P}}_n^{\tau m}(k) = \eta_n^m(k), \quad (42)$$

$$\frac{dT_n^m}{dt}(k) - \sum_{k'=1}^{kx}\Lambda_{k,k'}\bar{D}_n^{\tau m}(k) = \Theta_n^m(k), \quad (43)$$

$$\frac{dr_n^m}{dt}(k) = \Pi_n^m(k), \quad (44)$$

$$\frac{dq_n^m}{dt} + \bar{\bar{D}}_n^{\tau m} = M_n^m. \quad (45)$$

The "$-\tau$" notation over a variable indicates that it is to be evaluated implicitly. These prognostic spectral equations are evaluated at the full σ levels $k = 1, 2, \cdots kx$. The dependence of the spectral coefficients upon k is indicated by the notation "(k)", while their dependence upon time t is understood. Note that the spectral vorticity Eq. (41) and spectral water vapor Eq. (44) are fully explicit, whereas the spectral divergence Eq. (42), spectral thermodynamics Eq. (43) and spectral surface pressure Eq. (45) contain both explicit and implicit terms. The matrix coefficients $\Lambda_{k,k'}$ are independent of time and the spectral indices n and m.

The spectral hydrostatic equations have the same form as Eqs. (27a) and (27b). One merely replaces Φ_k by $\Phi_n^m(k)$, $T_v(k)$ by $T_{v_n}^m(k)$, etc. $\Phi_n^m(k)$ can be calculated explicitly from $T_{v_n}^m(k)$ or implicitly as described in the next section.

5. Semi-implicit time differencing scheme

A leapfrog semi-implicit time differencing scheme is used to approximate the time derivatives on the left-hand side of the spectral equations. We developed it independently, but it is very similar to Bourke's (1974) scheme. Analogous terms are treated implicitly in each scheme and a set of algebraic equations is solved for the spectral divergence coefficients $\bar{D}_n^{\tau m}(k)$. Relatively minor modifications arise due to the inclusion of the linearized virtual temperature.

For each value of n and m, there are kx coupled equations to be solved, of the form

$$\sum_{k'=1}^{kx}B_{k,k'}\bar{D}_n^{\tau m}(k') = J_k, \quad (46)$$

at levels $k = 1, \cdots kx$. Here J_k is an element of a column vector $\mathbf{J}$ which depends upon spectral co-

efficients with subscripts n and m at time t and $t - \Delta t$. Also, the $B_{k,k'}$ are elements of a matrix $\underset{\sim}{\mathbf{B}}$ of dimension kx by kx. The functional form of $B_{k,k'}$ is derived in Appendix B. The $\underset{\sim}{\mathbf{B}}$ matrix and its inverse $\underset{\sim}{\mathbf{B}}^{-1}$ depend upon the $\underset{\sim}{\mathbf{A}}$ matrix of Eq. (20) and upon the spectral index n, but not m. There are 61 distinct $\underset{\sim}{\mathbf{B}}$ matrices for the R30L09 spectral model, corresponding to the 61 values of n, i.e., 0, 1 $\cdots$ 60. $\underset{\sim}{\mathbf{B}}$ is independent of time as well, unless the time differencing scheme and/or time step are changed during the integration. In practice, leapfrog time differencing is used exclusively, except for a single Euler backward time step at the beginning of the integration. The standard time step for the R30L09 model is 20 minutes.

The inverse of the $\underset{\sim}{\mathbf{B}}$ matrices must be calculated only twice, i.e., during the Euler backward time step and during the first leapfrog time step. A Texas Instruments subroutine package is used for this purpose. Every time step, the right-hand side of Eq. (46) is multiplied by $\underset{\sim}{\mathbf{B}}^{-1}$ to obtain $\bar{D}_n^{\tau m}(k)$. The overhead for these computations is negligible.

Once $\bar{D}_n^{\tau m}(k)$ are known for $k = 1, \cdots kx$, $\bar{\bar{D}}_n^{\tau m}$ is readily calculated using Eq. (10). Also, $D_k(t + \Delta t) = 2\bar{D}_k^{\tau} - 2D_k(t - \Delta t)$, by definition of the semi-implicit operator. Moreover, knowledge of $\bar{D}_n^{\tau m}(k)$ and $\bar{\bar{D}}_n^{\tau m}$ enables us to calculate $T_n^m(k)$ in Eq. (43) and q_n^m in Eq. (45) at time $t + \Delta t$. In contrast, $\zeta_n^m(k)$ and $r_n^m(k)$ are determined at time $t + \Delta t$ by explicitly marching Eqs. (41) and (44) ahead in time.

After convectively adjusting $T_k(t + \Delta t)$ and $r_k(t + \Delta t)$, a Robert time filter is applied in the spectral domain to all the prognostic variables to prevent the solutions at even and odd time steps from decoupling. The filter has the form

$$Z_f(t) = (1 - 2\alpha)Z(t) + \alpha[Z(t + \Delta t) + Z_f(t - \Delta t)], \quad (47)$$

where the subscript f denotes a filtered value. Setting $\alpha = 0.03$, low frequency modes were only slightly damped (0.8% per day for $\Delta t = 15$ minutes and a mode with a period of 1 day).

The semi-implicit time differencing scheme with $\Delta t = 20$ min is obviously more efficient than the explicit leapfrog scheme with $\Delta t = 4.8$ min. However, we sought some assurance that the former would not adversely affect medium-range predictions. Therefore, comparative 10-day integrations were made with an hemispheric version of the R30L09 spectral model with full physics (similar to the "A2" package described in Section 6). All parameters were held fixed except the time differencing scheme and/or time step Δt. Three integrations were carried out: the standard τ-I integration (semi-implicit leapfrog time differencing and $\Delta t = 20$ min); τ-II (semi-implicit leapfrog and $\Delta t = 4.8$ min); and τ-III (explicit leapfrog and $\Delta t = 4.8$ min).

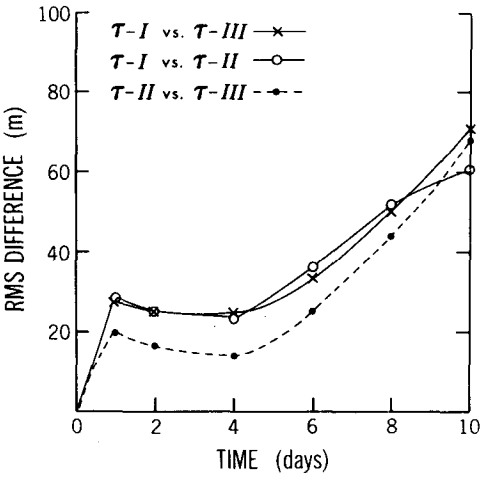

FIG. 1. Inter-model rms differences of z_{500} predictions from 1 January 1977 initial conditions vs time. The verification domain is 29–90°N. Model τ-I = semi-implicit, $\Delta t = 20$ min; τ-II = semi-implicit, $\Delta t = 4.8$ min; τ-III = explicit, $\Delta t = 4.8$ min.

The sensitivity of the medium-range prediction to the τ-I, τ-II and τ-III integrations was monitored. The results illustrated below are based on 1 January 1977 initial conditions. However, earlier integrations of an R30L09 global model with linear ∇^2 (instead of ∇^4) horizontal diffusion from 1 March 1965 initial conditions yielded qualitatively similar results.

Fig. 1 shows the time variation of the τ-I vs τ-III, τ-I vs τ-II and τ-II vs τ-III rms differences of predicted 500 mb geopotential height (z_{500}). The rms difference between τ-II and τ-III (semi-implicit, $\Delta t = 4.8$ min vs explicit, $\Delta t = 4.8$ min) is generally smaller than that between τ-I and τ-II or τ-I and τ-III for several days. This result is encouraging but does not prove that the two time-differencing schemes would converge for a very small time step. When verified against observations, τ-III had an rms error of 160 m at day 10 or $\sim$10 m less than τ-I (semi-implicit, $\Delta t = 20$ min). This difference is probably within the noise level. The model's natural variability level, i.e., the asymptotic rms difference between solutions corresponding to two randomly-chosen initial states, is $\sim$190 m.

The map comparison in Fig. 2 may be more informative. It shows that local differences between the τ-I and τ-III predictions of z_{500} are still very subtle at day 4, but not by day 10. However, the semi-implicit result is apparently no worse than the explicit, overall. In fact, the former may be regionally better. For example, on day 10, τ-I's ridge off the west coast of North America bears a closer resemblance to observation and its Hudson's Bay vortex is slightly more intense than τ-III's. The z_{1000} prediction at day 10 exhibited comparable sensitivity as the z_{500}.

A comparison of day 5–day 10 time-averaged precipitation (Fig. 3) is of some interest since the time

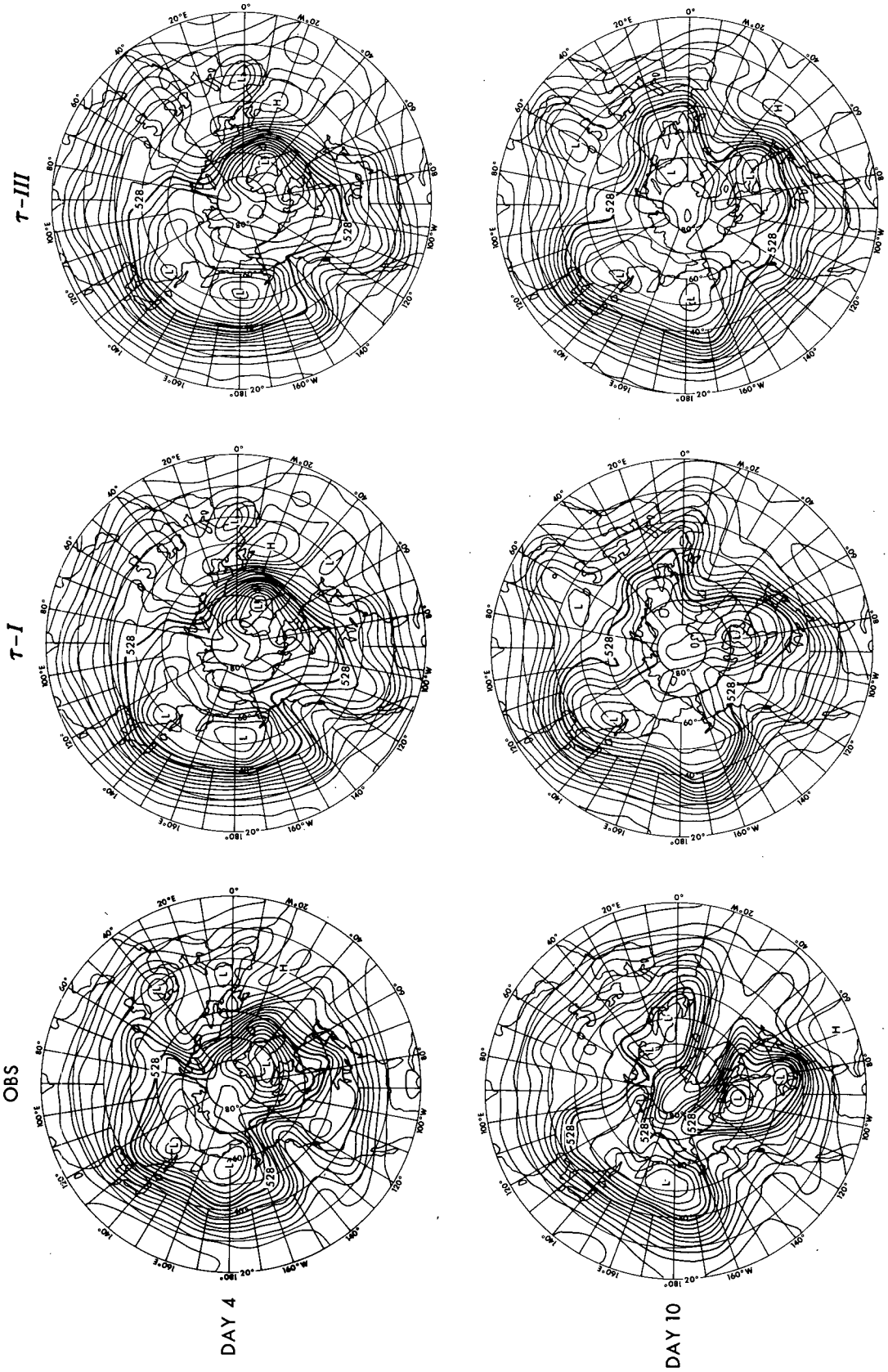

FIG. 2. Northern Hemisphere stereographic maps of z_{500} NMC observation (left), τ-I forecast (center) and τ-III forecast (right) for day 4 (top) and day 10 (bottom). Contour interval = 6 dam and reference contour = 552 dam.

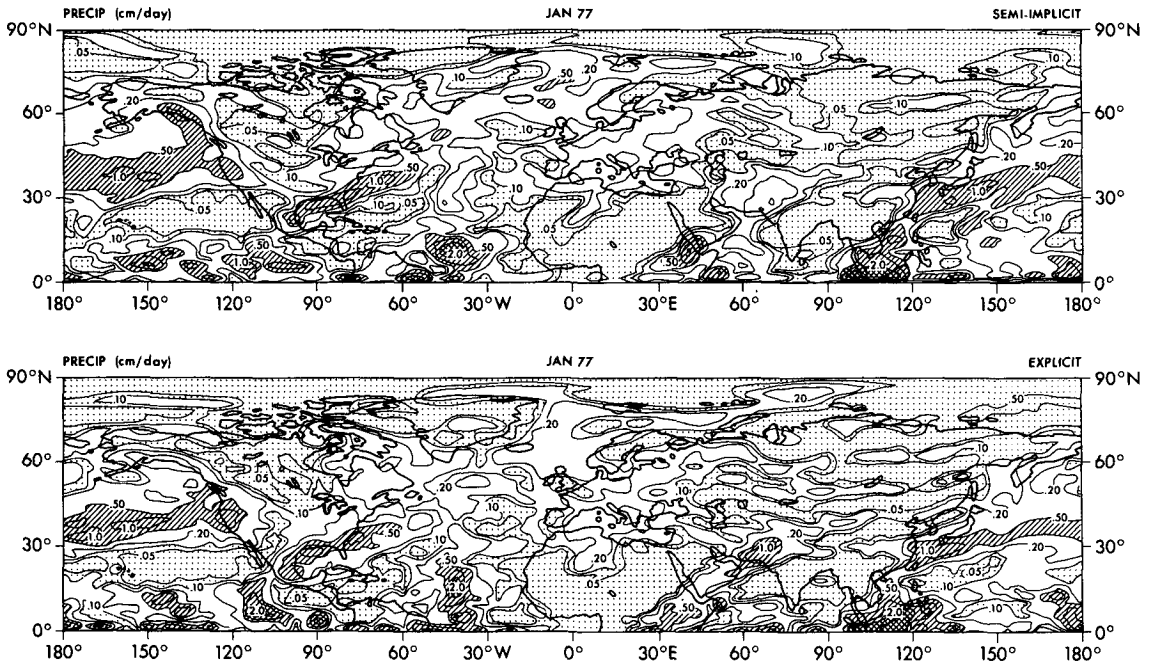

FIG. 3. Northern Hemisphere stereographic maps of τ-I (top) and τ-III (bottom) time-averaged precipitation rate r_p, for day 5–10, i.e., 6 January–11 January 1977. $r_p \leq 0.1$, $0.1 < r_p \leq 0.5$, $0.5 < r_p \leq 2.0$ and $2.0 < r_p$ cm day^{-1} in dotted, unshaded, hatched and cross-hatched regions, respectively.

intervals between convective adjustments and the numerical treatment of gravity-wave propagation are different in integrations τ-I and τ-III. Local differences between the τ-I and τ-III precipitation patterns can be detected in the tropics as well as extratropics. For example, the τ-III integration generates slightly more precipitation near the equator. Nonetheless, both precipitation patterns are quite similar.

In short, semi-implicit time differencing coupled with a 20 min time step did not appear to adversely affect the Jan 1977 (or March 1965) atmospheric prediction out to 10 days. Admittedly, the geopotential height prediction at day 10 was more sensitive to the time differencing scheme than we had envisioned. Yet, the 10 day prediction was considerably less sensitive to the time differencing scheme than to the domain (hemispheric vs global), horizontal resolution or sub-grid scale physics (E4 vs. A2, as defined in the next section). Perhaps the sensitivity to the time differencing scheme could be reduced by initializing the gravity wave modes more carefully.

6. Grid point physical processes

The physical processes of versions of the GFDL 2° resolution nine-level grid point model discussed by Miyakoda (1973) and Miyakoda and Sirutis (1977) have been adapted for the R30L09 spectral model. These versions are known as "A1", "A2" and "E4" physics, in order of increasing complexity. The "E4" physics option has only recently been incorporated into the spectral model. All three versions include horizontal diffusion, some form of vertical diffusion in the surface and planetary boundary layers, land–sea contrast, long- and shortwave radiative transfer, moist convective adjustment and treatment of soil moisture, and orography. Version "A1" is identical to "A2" except that in "A1", land–sea contrast does not include separate values of the surface drag coefficient for land and sea and the fractional surface wetness D_w is fixed at 0.5 over land instead of being predicted. As explained later, the essential difference between "A1" or "A2" physics and "E4" physics relates to the parameterization of vertical mixing in the surface boundary layer and above.

a. Horizontal diffusion

Enstrophy and kinetic energy are conserved by the spectral barotropic vorticity equation and approximately conserved by a multi-level, adiabatic, inviscid spectral model. This might suggest that there is less need for horizontal diffusion in spectral models than in certain grid point models when physical processes are incorporated. However, we have found that with horizontal diffusion, the medium range prediction of geopotential height is improved and the predicted spectral distributions of enstrophy and kinetic energy are more realistic.

In the GFDL spectral model, the standard scheme is a linear ∇^4 type of diffusion, i.e., the spectral ∇^2 operator is applied twice and a negative sign is placed

in front of the result. The (optional) linear ∇^2 scheme itself is based upon the analytic formulation on the sphere used by Bryan (1969). But the ∇^2 operator is spectrally computed and the $\hat{k}\cdot\nabla\times$ and $\nabla\cdot$ operators have been applied to the momentum diffusion. The coefficients of eddy diffusion for ∇^2 and ∇^4 were determined by trial and error, using the quality of the medium range 500 mb geopotential height forecast as a criterion.

Another option is a spectrally-computed nonlinear horizontal diffusion scheme. The Smagorinsky nonlinear scheme (Smagorinsky, 1963; Smagorinsky *et al.*, 1965) has handled the baroclinic scales quite successfully in moderate to high resolution finite difference models. It is somewhat less scale selective than the ∇^4 scheme but more selective than ∇^2. By the following analogy, it would seem that nonlinear *horizontal* diffusion would have a firmer physical basis than linear ∇^4 diffusion. Namely, nonlinear *vertical* diffusion, in contrast to linear $\partial^4/\partial z^4$, can be shown (Mellor and Yamada, 1974) to belong to a hierarchy of turbulent closure schemes.

In Smagorinsky's formulation, the horizontal eddy diffusion coefficient is proportional to the horizontal grid length and to the local deformation field. Although the spectral model's nonlinear diffusion scheme is conceptually similar to the GFDL grid point model scheme, horizontal finite differences are replaced by differentiation in the spectral domain. Thus the spectral character of the model is preserved. For simplicity, the spectral formulation is described on sigma levels. It has been generalized, however, to handle diffusion of heat and water vapor on pressure levels, by computing correction terms to the $\partial/\partial\lambda$ and $\partial/\partial\varphi$ derivatives of Eqs. (51) and (52) below. For example,

$$\left[\frac{\partial}{\partial\lambda}(\ )\right]_p = \left[\frac{\partial}{\partial\lambda}(\ )\right]_\sigma - \frac{\partial q}{\partial\lambda}\frac{[\Delta(\ )]_k}{(\Delta\sigma)_k}. \quad (48)$$

In the spectral model, this approach is more convenient and efficient than the (grid point model) technique of interpolating values from sigma levels to pressure levels.

The nonlinear horizontal diffusion terms common to both the spectral and grid point models at GFDL may be written as follows

$$F_{uH}\cos\varphi = \frac{1}{p_s}\left[\frac{1}{a}\frac{\partial}{\partial\lambda}(c_\lambda \hat{d} d_T) + \frac{1}{a\cos\varphi}\frac{\partial}{\partial\varphi}(c_\varphi \hat{d} d_s \cos^2\varphi)\right], \quad (49)$$

$$F_{vH}\cos\varphi = \frac{1}{p_s}\left[\frac{1}{a}\frac{\partial}{\partial\lambda}(c_\lambda \hat{d} d_s) - \frac{1}{a\cos\varphi}\frac{\partial}{\partial\varphi}(c_\varphi \hat{d} d_T \cos^2\varphi)\right], \quad (50)$$

$$F_{TH} = \frac{1}{\gamma_T p_s}\left[\frac{1}{a\cos\varphi}\frac{\partial}{\partial\lambda}\left(c_\lambda \hat{d}\frac{1}{a\cos\varphi}\frac{\partial T}{\partial\lambda}\right) + \frac{1}{a\cos\varphi}\frac{\partial}{\partial\varphi}\left(c_\varphi \hat{d}\frac{\cos\varphi}{a}\frac{\partial T}{\partial\varphi}\right)\right], \quad (51)$$

$$F_{rH} = \frac{1}{\gamma_r p_s}\left[\frac{1}{a\cos\varphi}\frac{\partial}{\partial\lambda}\left(c_\lambda \hat{d}\frac{1}{a\cos\varphi}\frac{\partial r}{\partial\lambda}\right) + \frac{1}{a\cos\varphi}\frac{\partial}{\partial\varphi}\left(c_\varphi \hat{d}\frac{\cos\varphi}{a}\frac{\partial r}{\partial\varphi}\right)\right]. \quad (52)$$

For simplicity, all reference to k has been suppressed for the variables F_{uH}, F_{vH}, d_T, d_s, $\hat{d}$, T and r. But $F_{uH} = F_{uH}(k)$, etc. The symbols in the above equations are as follows: F_{uH} and F_{vH} are the longitudinal and meridional components of the nonlinear horizontal diffusion of momentum $\mathbf{F}_{VH}$, F_{TH} and F_{rH} are the nonlinear horizontal diffusion of heat and water vapor, d_T and d_s are the tangential and shear deformation, $\hat{d}$ is the product of the surface pressure p_s with the vector magnitude of the tangential and shear deformation, the factors c_λ and c_φ are proportional to the square of the respective grid increments $\Delta\lambda$ and $\Delta\varphi$ on the transform grid and to an empirical constant k_0, and γ_T and γ_r are Prandtl numbers for sensible heat and water vapor transport.

The deformation-related variables d_s and d_T may be expressed in terms of the vorticity, divergence, and horizontal velocity components, i.e.,

$$d_s = \zeta + \mathcal{L}_1(u\cos\varphi)/\cos^2\varphi \quad (53)$$

and

$$d_T = D - \mathcal{L}_1(v\cos\varphi)/\cos^2\varphi, \quad (54)$$

where the linear differential operator

$$\mathcal{L}_1(\ ) = \left[\frac{\cos\varphi}{a}\frac{\partial}{\partial\varphi} + \frac{\sin\varphi}{a}\right].$$

Also,

$$\hat{d} = p_s(d_s^2 + d_T^2)^{1/2}. \quad (55)$$

Meanwhile, the factors c_λ and c_φ are given by

$$c_\lambda = \left(\frac{k_0}{\sqrt{2}}a\cos\varphi\Delta\lambda\right)^2 \quad (56a)$$

and

$$c_\varphi = \left(\frac{k_0}{\sqrt{2}}a\Delta\varphi\right)^2. \quad (56b)$$

Since $\Delta\lambda$ is a constant and since $\Delta\varphi$ is approximated by one, c_φ is a constant, whereas c_λ varies as $\cos^2\varphi$. By trial and error, 0.20 is thought to be a reasonable value of k_0 for the R30L09 spectral model. In comparison, $k_0 = 0.25$ is used in the GFDL 2° resolution nine-level global grid point model. In practice, the Prandtl numbers γ_T and γ_r are set equal to unity as in Miyakoda (1973).

As previously mentioned, an intermediate set of

transformations is carried out. First, the linear differential operator $\mathcal{L}_1$ is applied to the known spectral representations of $u\cos\varphi$ and $v\cos\varphi$. Next, $\mathcal{L}_1(u\cos\varphi)$, $\mathcal{L}_1(v\cos\varphi)$, ζ, D, $\cos\varphi\nabla T$ and $\cos\varphi\nabla r$ at levels $k = 1, \cdots kx$ and q at time $t - \Delta t$, (which are still in computer memory), are transformed to latitude $\varphi = \varphi_j$ and longitudes $\lambda_l = 2\pi l/L$, $l = 1, \cdots L$. There, the products $\hat{D}_s = \hat{d}d_s$ and $\hat{D}_T = \hat{d}d_T$, as well as

$$\hat{\mathbf{T}} = \hat{d}\cdot\left(\frac{c_\lambda}{a}\frac{\partial T}{\partial\lambda}\hat{\lambda} + \frac{c_\varphi}{a}\cos\varphi\frac{\partial T}{\partial\varphi}\hat{\varphi}\right)$$

and

$$\hat{\mathbf{r}} = \hat{d}\cdot\left(\frac{c_\lambda}{a}\frac{\partial r}{\partial\lambda}\hat{\lambda} + \frac{c_\varphi}{a}\cos\varphi\frac{\partial r}{\partial\varphi}\hat{\varphi}\right)$$

are computed ($\hat{\lambda}$ and $\hat{\varphi}$ are unit vectors in the λ and φ directions) and p_s is obtained by exponentiating q. Truncated spectral representations for the deformation-related variables $\hat{D}_s$, $\hat{D}_T$, $\nabla\cdot(\hat{\mathbf{T}}/\cos\varphi)$ and $\nabla\cdot(\hat{\mathbf{r}}/\cos\varphi)$ are obtained at levels $k = 1, 2, \cdots, kx$ at the completion of the grid to spectral transformation process.

The next step is to apply the linear differential operators

$$\mathcal{L}_2(\ \ ) = \left\{\frac{1}{a\cos\varphi}\frac{\partial}{\partial\varphi}[\cos^2\varphi(\ \ )]\right\}$$

$$= \left[\frac{\cos\varphi}{a}\frac{\partial(\ \ )}{\partial\varphi} - \frac{2\sin\varphi}{a}(\ \ )\right]$$

and

$$\mathcal{L}_3(\ \ ) = \left[\left(\frac{\Delta\lambda}{\Delta\varphi}\right)^2\frac{\cos^2\varphi}{a}\frac{\partial(\ \ )}{\partial\lambda}\right],$$

to $\hat{D}_s$ and $\hat{D}_T$ in the spectral domain. This yields spectral coefficients for $p_sF_{uH}\cos\varphi/c_\varphi$ and $p_sF_{vH}\cos\varphi/c_\varphi$. At this point, the main body of spectral to grid transformations are ready to be carried out. The spectral coefficients for $p_sF_{uH}\cos\varphi/c_\varphi$, $p_sF_{vH}\cos\varphi/c_\varphi$, $\nabla\cdot(\hat{\mathbf{T}}/\cos\varphi)$, $\nabla\cdot(\hat{\mathbf{r}}/\cos\varphi)$ and q are transformed to the grid point domain as well. After multiplying the first two variables by c_φ/e^q, we have

$$F_{uH}\cos\varphi = \frac{c_\varphi}{e^q}[\mathcal{L}_3(\hat{D}_T) + \mathcal{L}_2(\hat{D}_s)], \quad (57)$$

$$F_{vH}\cos\varphi = \frac{c_\varphi}{e^q}[\mathcal{L}_3(\hat{D}_s) - \mathcal{L}_2(\hat{D}_T)]. \quad (58)$$

Similarly, the equations

$$F_{TH} = \frac{\nabla\cdot(\hat{\mathbf{T}}/\cos\varphi)}{\gamma_T e^q}, \quad (59)$$

$$F_{rH} = \frac{\nabla\cdot(\hat{\mathbf{r}}/\cos\varphi)}{\gamma_r e^q}, \quad (60)$$

are formally equivalent to Eqs. (51) and (52), respectively. This may be shown by substituting the expressions for $\hat{\mathbf{T}}$ and $\hat{\mathbf{r}}$ into the latter equations and expanding the divergences in the manner of Eq. (34a). The grid point values of F_{uH} and F_{vH} and hence $\mathbf{F}_{VH}(k)$ contributes to $\mathbf{F}_{VN}(k)$. Likewise, F_{TH} contributes to $F_{TN}(k)$ and F_{rH} to $F_{rN}(k)$. These contributions are added to the other nonlinear terms which affect $\mathbf{S}_k$ in Eq. (13), $\Theta_N(k)$ in Eq. (18) and μ_k in Eq. (24).

Some higher-order aliasing is anticipated since $\hat{D}_s$, $\hat{D}_T$, $\hat{\mathbf{T}}$ and $\hat{\mathbf{r}}$ are not elementary quadratic products of two spectrally truncated variables. But higher-order aliasing is generally negligible (Bourke *et al.* 1977).

One desirable property of the nonlinear horizontal diffusion scheme is that it generates no frictional torques when applied to a uniformly rotating flow. The proof involves showing that $d_s = 0$ in Eq. (53) and $d_T = 0$ in Eq. (54) and hence $\hat{d} = 0$. Secondly, although the derived deformation fields d_s and d_T do not have spherical harmonics representations in closed form, they are finite at the pole. To prove this, one expresses d_T and d_s in terms of the streamfunction ψ and velocity potential χ, and P_n^m as a linear combination of the elementary trigonometric functions $\cos^{|m|}\varphi\sin^{n-|m|-2j}\varphi$, $j \leqslant n - |m|/2$. Then, if one differentiates the finite spectral expansions of ψ and χ term by term, the apparent singularity at the poles due to the $\cos^{-2}\varphi$ factor in Eqs. (53) and (54) vanishes.

Ten day comparative integrations were performed to see if any of the horizontal diffusion schemes, i.e., nonlinear, linear ∇^4 or linear ∇^2 was clearly superior to the others. The preliminary indications were inconclusive. In any case, ∇^4 diffusion was selected as the standard scheme for its scale selectivity and computational efficiency.

b. *Surface exchange*

In model versions "A1" and "A2", vertical diffusion in the surface boundary layer beneath level kx is governed by bulk aerodynamic drag laws, i.e., the wind stress is $-c_D|\mathbf{V}_{kx}|\mathbf{V}_{kx}$, the surface sensible heat flux $-c_D|\mathbf{V}_{kx}|(\theta_{kx} - \theta_s)$ and the surface evaporation $-c_D D_w|\mathbf{V}_{kx}|[r_{kx} - r_{\text{sat}}(T_s)]$. Here, c_D is the surface drag coefficient, D_w is the fractional surface wetness, θ is the potential temperature, the "s" subscript denotes surface values and r_{sat} is the surface saturation mixing ratio.

Meanwhile, in the "E4" physics version, the vertical diffusion is governed by the Monin-Obukhov formulation, as in Delsol *et al.* (1971). The latter formulation is based upon the similarity hypothesis and is dependent upon static stability. The Monin-Obukhov length is currently solved by an iterative method. Heat conduction through the soil is included in the surface heat balance and the surface roughness z_* over the ocean is calculated by Charnock's formula $z_* = 0.032\ u_*/g$, where u_* is the so-called friction velocity.

c. Vertical diffusion in the planetary boundary layer

In the "A" physics packages, momentum and water vapor are diffused vertically in the planetary boundary layer in accordance with mixing length theory for a neutrally stratified atmosphere. Thus, the eddy coefficients K_m and K_r for vertical diffusion of momentum and water vapor are proportional to the magnitude of the local vertical wind shear and to the mixing length. The latter decreases linearly from ~30 m at level σ_9 to zero at level $\sigma_{5+1/2}$. Following Miyakoda (1973), we set K_r equal to K_m. Meanwhile, $K_T = 0$, i.e., the vertical subgrid-scale sensible heat transport is accomplished entirely by convective adjustment. In other words, it is completely suppressed if the stratification is stable.

"E4" physics has two distinctive facets in the planetary boundary layer (and free atmosphere). First, dry convective adjustment is suppressed. Second, vertical diffusion is calculated in accordance with the Mellor-Yamada (1974) level 2.5 turbulent closure scheme, which is Richardson-number-dependent. Accordingly, to obtain the eddy diffusion coefficients, a prognostic equation is solved for the turbulent kinetic energy only, whereas the other second-order moments are calculated diagnostically. Further details of the scheme may be found in Miyakoda and Sirutis (1977).

d. Land–sea contrast

This refers to the different specifications of surface temperature and different values of surface drag over land, sea and sea ice. Monthly mean sea-surface temperature data prepared by the Rand Corporation and coastlines consistent with topography data prepared by the Scripps Institution of Oceanography are interpolated directly from a $1 \times 1°$ latitude–longitude grid to the model's transform grid. The surface temperature over land is determined by solving a surface heat balance equation which includes short- and long wave radiative fluxes, sensible heat flux and latent heat flux. If the calculated surface temperature over snow-covered land exceeds 273.2 K, the excess heat is used to melt snow. Unless otherwise indicated, the surface temperature over sea ice is calculated from a surface heat balance equation which includes heat conduction through a specified ice thickness (currently 2 m) in addition to the various fluxes computed over land. The surface drag coefficient in the "A2" physics version is set to 0.0043 over land and 0.0011 over the water and sea ice, while the Prandtl number equals 1.0 everywhere. In the "A1" physics version, $c_D = 0.0020$ everywhere. Although surface temperature is formally an untruncated grid point field, the surface heat flux contribution to the spectral temperature tendency is, in effect, spectrally truncated.

e. Radiation

The standard Manabe-Strickler (1964) long- and shortwave radiative transfer algorithms of the GFDL 2° resolution grid point model have been incorporated into the spectral model. The standard specification for the radiatively active constituents consists of climatological zonal mean values. A different climatology is available each season for ozone, water vapor and cloudiness, whereas the carbon dioxide climatology is fixed. Seasonal means of the latitude-dependent solar zenith angle are specified as well. However, the following options may be selected: 1) seasonal variation of ozone, water vapor, cloudiness and solar zenith angle; 2) diurnal variation of the incoming solar radiation; 3) use of model-predicted water vapor in the radiation calculation; and 4) the more efficient and supposedly more accurate radiative transfer algorithms developed by Fels and Schwarzkopf (1975). Miyakoda *et al.* (1982) summarize the highlights of the Fels-Schwarzkopf scheme.

f. Convective adjustment and hydrologic cycle

The hydrologic aspects of the spectral model are taken from the GFDL grid point model. For example, convective and large-scale precipitation are parameterized on the transform grid using the Manabe *et al.* (1965) dry and moist convective adjustment/large scale condensation scheme with an 80% saturation criterion for condensation. In both the "A2" and "E4" physics version, evaporation, precipitation and snow melt affect soil moisture in the ground branch of the hydrologic cycle. In turn, the fractional surface wetness and hence surface evaporation are influenced by the soil moisture (Manabe, 1969).

Whereas regions of negative mixing ratio are generated and must be controlled even in the grid point model, they pose a somewhat greater nuisance in the spectral model. First, the spectral truncation process itself generates negative values, particularly in low resolution models. Also, regions of negative mixing ratio may expand, apparently as a consequence of spectral truncation.

In the grid point model, the negative mixing ratio problem is controlled by vertical borrowing and residual borrowing. Vertical borrowing is performed at a grid point if its mixing ratio is negative and the combined mixing ratio of its nearest vertical neighbors equals or exceeds the deficit. In this case, the negative value is reset to zero and the borrowed amount is subtracted from the donors so as to conserve the total water in the vertical column. All remaining negative mixing ratios are simply reset to zero without regard to local conservation of water vapor on horizontal surfaces. This residual borrowing process creates a spurious but rather negligible source of water vapor in the 2° resolution grid point

model. Unfortunately, the spurious source is approximately a factor of 30 greater in the R30 spectral model. An undesirable side effect of residual borrowing pointed out to us by S. Manabe (personal communication, 1978) is the generation of excess water vapor and hence excess precipitation in the polar region. This problem is not alleviated by imposing conservation of the global mean mixing ratio during the residual borrowing process.

Consequently, residual borrowing was replaced by local horizontal borrowing based upon the same principles as the vertical borrowing scheme. In particular, remaining negative mixing ratios are left alone unless the nearest east–west neighbors have enough water vapor to make up the deficit. It appears that the excessive rate of precipitation near the poles is somewhat reduced, whereas the areal extent of weakly negative mixing ratios is slightly larger. Such a tradeoff would be favorable.

7. Orography

Spherical harmonic spectral coefficients of the earth's topography are computed from grid point surface elevation data. Two data sets were available, i.e., topography on a 1° resolution latitude–longitude grid prepared by the Scripps Institution of Oceanography and the GFDL grid point model's topography on the 2° resolution modified Kurihara grid. The Scripps topography was chosen because it contains more variance. Local smoothing with a Gaussian distribution was applied to the Scripps data in the course of interpolating it to the desired transform grid. The smoothing parameters were dependent upon the resolution of the transform grid.

Although the smoothing procedure is rather ad hoc, we were guided by two principles: 1) the variance of the smoothed data should be as faithful as possible to the observations without generating excessive amplitude gravity waves. 2) Local smoothing of the original data is preferable to post-filtering of the spherical harmonic spectral coefficients. The final re-synthesized R30 spectral topography field contains negative values which are as large as 200 m near the Antarctic coast. Weaker amplitude noise patterns are found over the oceanic regions as well.

8. Computational requirements

Computational efficiency is very sensitive to the per cent of vectorized code on the ASC computer. Therefore, considerable effort was made to vectorize the GFDL spectral model code as well as specify the do-loop parameters at compilation time. On the other hand, we have not written any machine language code. Fig. 4 illustrates the cpu time requirements on the ASC computer for various components of the R30L09 spectral model. The estimates apply to a 1-day run with semi-implicit time differencing and $\Delta t = 20$ min. We see that the Fourier and Legendre-related transforms for the dynamics take little time relative to the grid point physical processes—especially diffusion and radiation. The adiabatic and inviscid R30L09 global model, including transforms and grid point dynamics, requires 7.5 min of ASC CPU time for a one day forecast. The twice-daily standard Manabe-Strickler radiation code consumes ~10 min of CPU time [in contrast to 3 min by the Fels-Schwarzkopf (1975) scheme]. Meanwhile, the "A2" physics package including surface heat balance requires over 2 min, dry and moist convective adjustment over 4 min, and optional nonlinear horizontal diffusion 6.5 min. It takes 16 min of CPU time more per model day to compute "E4" physics than "A2" physics in the R30L09 model. However, more efficient algorithms for "E4" are being developed. Integration of the R30L09 model with "A2" physics (including ∇^4 horizontal diffusion and the Manabe-Strickler radiation code) requires ~25 min of CPU time per model day. The corresponding figure for the R30L09 model with "E4" physics and nonlinear horizontal diffusion is 47 min. Explicit time differencing would increase the R30L09, "A2", ∇^4 model's running time to 64 min. A 1-day integration of the R60L09 hemispheric spectral model with "A2" physics, ∇^4 horizontal diffusion, standard radiation code and $\Delta t = 10$ min requires 95 min of CPU time.

9. Applications of spectral models at GFDL

Post-1974 versions of the GFDL spectral prediction model have recently been adapted and applied, within GFDL to research in such diverse areas as extended and long range atmospheric prediction, four-dimensional assimilation of data, climate, and planetary atmospheres. In fact, the feasibility of various studies hinged upon the spectral model's computational efficiency combined with its reasonable accuracy at R15 to R30 spectral resolution. We also note that much of the above research is about to be published. Therefore, a short review of applications of spectral models at GFDL should be timely as well as useful. The applications of spectral models and their resolution characteristics are listed in Table 2.

a. Extended and long range prediction

Miyakoda *et al.* (1979) focused on the cumulative results of extended range predictions by a 2.25° resolution, nine-level hemispheric grid point model with "A" type physics, for 10 summer cases. However, based upon three cases, the R30L09 spectral model performed at least as well as the grid point model, if not slightly better out to 10 days. A detailed comparative evaluation between an R30L09 global spec-

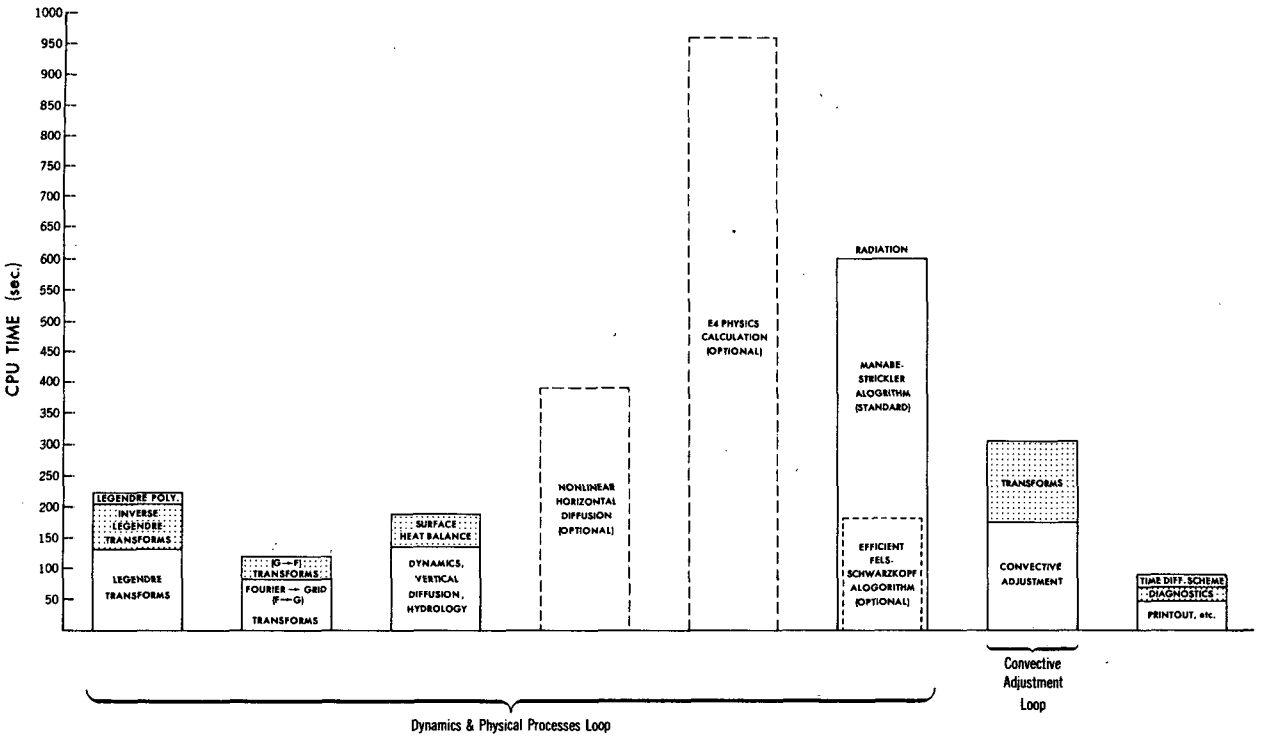

FIG. 4. Bar graph of CPU time estimates (in seconds) for a 1 day integration of the global R30L09 spectral model, partitioned according to model process. Solid bars indicate standard processes and dashed bars model options. Semi-implicit time differencing and a 20 min time step are assumed.

tral and the so-called N48L09 global grid point model for three winter cases will be reported on in a forthcoming paper. The latter model has a modified Kurihara grid (Umscheid and Bannon, 1977) with 48 grid points between pole and equator (1.9° meridional resolution) as well as nine sigma levels. The grid point model has somewhat higher resolution than the R30L09 transform grid, particularly in the tropics. Both models have "A" type physics. The integrations were extended out to 15 days. The spectral model tended to predict the phase of transient disturbances more accurately. However, in at least one case the R30L09 quasi-stationary planetary-scale waves lost amplitude, relative to the N48L09, after 8–10 days, although even the N48L09 amplitude was deficient. The R30L09 planetary-scale wave amplitudes were noticeably enhanced, however, when "E4" physics was used.

Thirty day simulations of a January 1977 blocking event have been carried out (K. Miyakoda, personal communication, 1982) with an N48L09 E4, N48L09 A2, R30L09 E4 and an R30L09 A2 model. "E4" physics appears to be a crucial factor for maintaining the blocking patterns in the vicinity of North America out to 25 or 30 days for reasons as yet unexplained. The N48L09 E4 prediction was the most successful. We hope that spectral models will eventually be accurate enough to predict 30-day means and perhaps 10-day means of the geopotential height field up to two or three months in advance.

b. Four-dimensional assimilation

The spectral model is an important component of the GFDL four-dimensional optimal analysis system used for processing FGGE data. A technique for assimilating data into a spectral model was developed by Simmonds (1976) and applied to a barotropic spectral model. Prior to insertion of data, the model's spectral variables are transformed to the grid point domain. Data are then inserted whenever available. Finally, the resulting hybrid field is transformed to the spectral domain and spectrally truncated before resuming the integration. This technique was also successfully applied by Simmonds (1978) to two versions of the GFDL R30L09 spectral prediction model, i.e., one with "A" type physics and one with more limited physical processes. A much more complicated system, comprised of pre-processing, four-dimensional assimilation, univariate optimal interpolation (OPI) statistical analysis, and nonlinear normal mode initialization was developed at GFDL to generate FGGE analyses. An R30L18 global spectral model is used for the four-dimensional assimilation and nonlinear normal mode initialization. The model incorporates the Monin-Obukhov formulation

for the surface boundary layer, the Fels-Schwarzkopf (1975) radiation algorithms and solar diurnal variation.

The assimilation of data is accomplished in a series of steps. Asynoptic data and timely synoptic data are grouped into time blocks of two hours and vertically interpolated to a set of standard pressure levels. The latter data are optimally interpolated to the R30 transform grid, using the most recent (0000 or 1200 GMT) meteorological analysis as a first guess. Next, the horizontal OPI analysis is vertically interpolated to the model sigma surfaces. Finally, the model solution is replaced by grid point insertion data, which is a weighted combination of the OPI analysis and the present model solution. The weights depend upon various factors including the type and reliability of the original synoptic and asynoptic data. To enhance the assimilation of the data, the insertion process is repeated each time step using the same OPI analysis over a particular 2 h interval. It is interesting to note that the ECMWF scheme employs a 6 h forecast–OPI analysis cycle (Lorenc, 1981). Thus, the OPI analysis affects the final analysis more directly in the ECMWF, as compared to the GFDL data analysis system.

In the present GFDL system, nonlinear normal mode initialization is applied at 6 h intervals, just after the archival, if performed, of a final four-dimensional analysis. The main benefit is better control of small-scale noise. The GFDL scheme is based on the formulation of Machenhauer (1977). Six iterations were found to provide optimal convergence. Also, only the first seven vertical modes of the R30L18 spectral model are initialized. A novel feature of the GFDL scheme is that slow modes with periods exceeding 6 h, are not initialized. This frequency cutoff criterion is more severe than the vertical modes cutoff criterion. Its primary function is to help preserve the amplitude of the tropical (Hadley) meridional circulation. The slow modes, which tend to be forced in the tropics by diabatic heating, would be adversely affected by the application of nonlinear normal mode initialization.

Perhaps the most important conclusion reached thus far, is that four-dimensional assimilation is a viable alternative to the forecast-OPI analysis cycle approach. In particular, it does not significantly reduce the amplitude of midlatitude, synoptic scale disturbances or generate excessive small scale noise provided that: 1) climatology is not the first guess field for the OPI and 2) the "data toss-out" criterion in the OPI is not too severe. The GFDL/FGGE analysis system is described in more detail by Miyakoda *et al.* (1982).

Although it takes ~3.0 h of CPU time on the ASC computer to process and analyze one day of FGGE data, the computations would not have even been feasible with the N48L18 grid point model. On the other hand, the analyses would have been of inferior quality if the coarser resolution N24L18 model had been used.

c. Climate

The GFDL spectral prediction model has been adapted by L. Holloway of the climate group for climate simulation studies. In effect, he linked our spectral-grid dynamics and semi-implicit time differencing scheme to a GFDL climate model. Despite differences in long-period forcings, condensation criterion and placement of the sigma levels, the prediction and climate models are rather similar. The climate model versions with R15, R30, T21 and T30 spectral resolution have been integrated using linear ∇^4 horizontal diffusion with $\nu \approx 1.0 \times 10^{16}$ m^4 s^{-1} or occasionally $\nu \approx 2.5 \times 10^{15}$ m^4 s^{-1}. An intercomparison of the R15, R21 and R30 results is reported in Manabe *et al.* (1979). For climate simulation purposes, the R15L09 model version is quite respectable. For example, it simulates the sea level pressure field better than a comparable 500 km resolution grid point model, yet is far more economical. Increasing the resolution to R30L09, the sea-level pressure simulation becomes more realistic in the Southern Hemisphere. But the belt of surface westerlies in the Northern Hemisphere becomes too intense in winter. Meanwhile, the precipitation belts and dry zone are simulated better as the resolution is increased. In any case, the use of the R15L09 spectral climate model for climate variability and climate sensitivity studies appears justifiable.

Manabe and Hahn (1981) and Lau (1981) have analyzed the time variability of a 15-year integration of the R15L09 spectral model. Topography, seasonally varying sea-surface temperature and insolation, snow–albedo feedback and soil moisture feedback were included in the model. But no non-seasonal perturbations were introduced into the prescribed forcing. Manabe and Hahn noted that the variability of both the daily and monthly mean 1000 mb geopotential height field were well-simulated at midlatitudes. However, the monthly mean variability was somewhat too weak in the tropics. Lau has focused on the three-dimensional structure and temporal behavior of the most prominent circulation anomalies appearing in the R15L09 integration. For this purpose, he employed a wide variety of techniques including empirical orthogonal function representations, teleconnection patterns and frequency spectra. The large-scale features of the model's anomaly patterns were internally consistent, qualitatively similar to the predominant observed standing modes, and had a characteristic time scale of 15–20 days. On the other hand, Lau found that the model was unable to simulate the east–west sea-level pressure seasaw associated with the observed Southern

Oscillation. He speculated, as Manabe and Hahn (1981) had done, that a lack of air–sea coupling might be the cause.

As a next step, R. N. Keshavamurty (personal communication, 1981) has investigated the sensitivity of the R15L09 climate model simulation to imposed warm sea-surface-temperature anomalies in the equatorial Pacific. Although a complete air–sea coupling was absent, he was able to simulate different phases of the observed Walker circulation. The phase essentially depended on the region where the sea-surface-temperature anomalies were placed. Also, dynamically consistent atmospheric circulation anomalies did indeed rise above the natural variability "noise" level of the model.

In an unrelated study, Meleshko and Wetherald (1981) have analyzed the sensitivity of a 60-day integration of the R21L09 spectral climate model to the fixed cloud distribution. Seasonal parameters appropriate to Northern Hemisphere summer were prescribed. Also, two cloud distributions, one zonally symmetric, the other geographical, were specified. The latter was generated by a scheme which incorporates longwave radiation fluxes measured by satellites. The geographical cloud distribution caused the surface temperature to increase by 2 to 4 K over the continents, but the sea-surface temperatures were held fixed. The surface pressure decreased over the continents (by as much as 12 mb at midlatitudes) and increased over the oceans.

In yet another study, Wetherald and Manabe (1981) have analyzed the sensitivity of the R15L09 spectral climate model to the quadrupling of the carbon dioxide concentration. Their atmospheric model excluded topography but was coupled to a simple mixed layer ocean model. The domain was an arbitrary 120° sector. They found that the climate is much less sensitive to carbon dioxide if the seasonal variation of the solar insolation at the top of the atmosphere is imposed. In this case, the highly reflective snow cover at polar latitudes disappeared in summer, thereby reducing the sensitivity.

d. Planetary atmospheres

Thus far, there have been two applications of the GFDL spectral prediction model in this area. First, W. Rossow has constructed an R15L09 spectral model with parameters (e.g. radius, retrograde rotation rate and mass) appropriate for the Venusian atmosphere. The model extends from the surface to 70 km, i.e., near the top of the observed cloud layer. Rossow removed all the physical processes except for dry convective adjustment and ∇^2 horizontal diffusion, then added Newtonian heating based upon an assumed equilibrium temperature profile. The above model was integrated out to 5000 days. The results have appeared in condensed form in Rossow (1978, 1979). In Rossow's model, the larger scale modes have a more predominant influence than convective scale modes upon the temperature structure. An intense, thermally direct Hadley cell develops 50–70 km above the surface and a weaker direct cell in the lowest 10 or 20 km. The mean stratification remains weakly stable. Rossow's vertical profile of the zonal wind agrees qualitatively with Pioneer satellite observations in the 10–20 km region. However, he has not yet successfully simulated the so-called 4-day wind by prescribing diurnal-varying radiative forcing.

Second, Williams and Holloway (1982) have investigated the response of the atmospheric general circulation of an earthlike planet to variations in rotation rate and obliquity. For this purpose, Holloway constructed an R15L09 and an R42L09 sector model, among others, from the GFDL climate group's spectral model with "A" physics. Many aspects of the simulated general circulation qualitatively resembled that of the Venusian, Martian or Jovian atmospheres when the rotation and obliquity parameters appropriate to those planets were specified. Their results suggest that these two parameters strongly influence the circulation of planetary atmospheres. Also, at low rotation rates, the diurnal variation in the solar heating plays an important role.

10. Concluding remarks

A global spectral transform model, developed at GFDL, has been described in detail. This model was originally designed for carrying out extended range prediction experiments. However, it has also been adapted and applied to the four-dimensional assimilation of data, climate studies and simulation of the Venusian atmosphere.

The spectral aspects, semi-implicit time differencing scheme and grid point physical processes of the model were emphasized. Two apparently unique features of the GFDL spectral prediction model are its linearized virtual temperature correction and an optional spectrally-computed nonlinear horizontal diffusion scheme.

The basic model has R30L09 resolution and utilizes the so-called "A2" physics package and linear ∇^4 horizontal diffusion. Its capability at extended range prediction, i.e., 10 days and beyond, will be discussed in a forthcoming paper. Concerning other model versions, preliminary results from the more advanced R30L09 "E4" spectral model are quite encouraging. More specifically, the "E4" physics appears to improve the quality of the R30L09 medium range forecast. Also, the integration of a global R42L09 "E4" model and a hemispheric R60L09 "A2" model are in progress. An R30L18 spectral model is playing a prominent role in the production of four-dimensional analyses of FGGE data at GFDL. Finally, lower resolution spectral models are being widely used in climate sensitivity studies.

Acknowledgments. We are grateful to Dr. K. Miyakoda for his continuing encouragement. Dr. Kurihara, Dr. K. Miyakoda and J. L. Holloway kindly read the manuscript and offered valuable suggestions. Thanks go to Betty M. Williams for typing the manuscript, P. G. Tunison for drafting the figures and J. N. Connor for photographing them.

APPENDIX

Derivation of the $B_{k,k}$ Matrix Elements

The semi-implicit leapfrog time differencing scheme is applied in the spectral domain. For simplicity, the spectral indices n and m will usually be suppressed in the course of the derivation; factors involving n or m will be retained, however. For example, $n(n+1)D_n^m(k)$ would be written as $n(n+1)D_k$.

Before carrying out the derivation, it is useful to define the semi-implicit operator associated with leapfrog time differencing. If it is applied to an arbitrary variable Z, then

$$\bar{Z}^{\tau} = [Z(t+\Delta t) + Z(t-\Delta t)]/2, \qquad \text{(A1)}$$

where t is the time and Δt is the time step. Thus, the leapfrog time differencing operator may be written as

$$\frac{\delta Z}{\delta t} = [\bar{Z}^{\tau} - Z(t-\Delta t)]/\Delta t. \qquad \text{(A2)}$$

For fixed n and m, a set of kx algebraic equations for the kx spectral coefficients $\bar{D}_k^{\tau}$, $k = 1, kx$ may be obtained as follows: First, the spectral divergence equation (42) at level $k+1$ is subtracted from its counterpart at level k, $1 \leq k \leq kx-1$. Then, applying the finite difference operator (A2) to this intermediate equation as well as to the divergence equation at level $k = kx$, we obtain

$$\bar{D}_k^{\tau} - \bar{D}_{k+1}^{\tau} - \frac{n(n+1)}{a^2}(\bar{\hat{P}}_k^{\tau} - \bar{\hat{P}}_{k+1}^{\tau})\Delta t = I_k, \qquad \text{(A3a)}$$

$k = 1, \cdots kx-1$ and

$$\bar{D}_{kx}^{\tau} - \frac{n(n+1)}{a^2}\bar{\hat{P}}_{kx}^{\tau}\Delta t = I_{kx}. \qquad \text{(A3b)}$$

Here, I_k is shorthand notation for $D_k(t-\Delta t) - D_{k+1}(t-\Delta t) + (\eta_k - \eta_{k+1})\Delta t$, and I_{kx} for $D_{kx}(t-\Delta t) + \eta_{kx}\Delta t$. Second, the $\bar{\hat{P}}_k^{\tau}$ spectral coefficients must be eliminated from Eqs. (A3a) and (A3b). The lengthy manipulations may be summarized as follows:

i) Eq. (A2) is applied to $\bar{\hat{P}}_k^{\tau}$ to obtain

$$\bar{\hat{P}}_k^{\tau} = \frac{\delta \hat{P}_k}{\delta t}\Delta t + \hat{P}_k(t-\Delta t).$$

ii) The leapfrog finite difference operator is applied to Eq. (40) to obtain

$$\frac{\delta \hat{P}_k}{\delta t} = \frac{\delta \Phi_k}{\delta t} + R\bar{T}_v(k)\frac{\delta q}{\delta t} \qquad \text{(A4)}$$

and Eq. (A4) is used to eliminate $\delta \hat{P}_k/\delta t$. Note that $\hat{P}_k(t-\Delta t)$ is known.

iii) $(\delta\Phi_k/\delta t) - (\delta\Phi_{k+1}/\delta t)$ and $\delta\Phi_{kx}/\delta t$ are expressed as linear combinations of $\delta T_v(k)/\delta t$ and $\delta T_v(k+1)/\delta t$ and of $\delta T_v(kx)/\delta t$ and $\delta T_v(kx-1)/\delta t$, respectively, using Eqs. (27b) and (27a). In turn,

$$\frac{\delta T_v(k)}{\delta t} = \frac{\delta T_k}{\delta t} + 0.61\bar{T}_v(k)\frac{\delta r_k}{\delta t}.$$

iv) The leapfrog finite difference approximations to dT_k/dt, dr_k/dt and dq/dt are replaced by their respective spectral tendencies, i.e., by the right-hand side of the spectral thermodynamics Eq. (43), water vapor Eq. (44) and surface pressure Eq. (45).

The final result, in matrix form, is the kx coupled linear equations

$$\sum_{k'=1}^{kx} B_{k,k'}\bar{D}_{k'}^{\tau} = I_k + \frac{n(n+1)}{a^2}\Delta t G_k, \qquad \text{(A5)}$$

for the kx unknowns $\bar{D}_k^{\tau}$, or more precisely $\bar{D}_n^{m\tau}(k)$, $k = 1, 2 \cdots kx$, where n and m are fixed. The matrix elements are given by

$$B_{k,k'} = \frac{n(n+1)}{a^2}(\Delta t)^2\{\alpha_k\Lambda_{k,k'} + \beta_k\Lambda_{k+1,k'} + R[\bar{T}_v(k) - \bar{T}_v(k+1)](\Delta\sigma)_{k'}\} + \delta_{k,k'} - \delta_{k+1,k'}, \qquad \text{(A6a)}$$

for $k = 1, 2, \cdots kx-1$; and

$$B_{kx,k'} = \frac{n(n+1)}{a^2}(\Delta t)^2[\hat{\alpha}\Lambda_{kx,k'} + \hat{\beta}\Lambda_{kx-1,k'} + R\bar{T}_v(kx)(\Delta\sigma)_{k'}] + \delta_{kx,k'}, \qquad \text{(A6b)}$$

where

$$\delta_{k,k'} = \begin{cases} 1 & \text{if } k' = k \\ 0 & \text{if } k' \neq k. \end{cases}$$

The right-hand side of Eq. (A5) was denoted by J_k in Eq. (46) in Section 5. Also, in Eq. (A5), G_k is the expression

$$G_k = \{\hat{P}_k - \hat{P}_{k+1} + \alpha_k T_v(k) + \beta_k T_v(k+1) + R[\bar{T}_v(k) - \bar{T}_v(k+1)]q\}_{t-\Delta t} + \{\alpha_k(\Theta_k + 0.61\bar{T}_k\Pi_k) + \beta_k(\Theta_{k+1} + 0.61\bar{T}_{k+1}\Pi_{k+1}) + R[\bar{T}_v(k) - \bar{T}_v(k+1)]M\}\Delta t \qquad \text{(A7a)}$$

for $k = 1, 2, \cdots, kx-1$; and for $k = kx$,

$$G_{kx} = [\hat{P}_{kx} + \hat{\alpha}T_v(kx) + \hat{\beta}T_v(kx-1) + R\bar{T}_v(kx)q]_{t-\Delta t} + [\hat{\alpha}(\Theta_{kx} + 0.61\bar{T}_{kx}\Pi_{kx}) + \hat{\beta}(\Theta_{kx-1} + 0.61\bar{T}_{kx-1}\Pi_{kx-1})]\Delta t. \qquad \text{(A7b)}$$

REFERENCES

Baede, A. P. N., and A. W. Hansen, 1977: A ten-day high resolution nonadiabatic spectral integration: A comparative study. European Centre for Medium Range Forecasts, Tech. Rep. No. 7, 82 pp.

Boer, G. J., and N. A. McFarlane, 1978: A January simulation using the AES atmospheric general circulation model. Canadian Climate Centre, Atmospheric Environment Service, Internal Rep. No. 1, 53 pp.

Bourke, W., 1972: An efficient, one-level, primitive-equations spectral model. *Mon. Wea. Rev.*, **100,** 683–689.

——, 1974: A multi-level spectral model I. Formulation and hemispheric integrations. *Mon. Wea. Rev.*, **102,** 687–701.

Bourke, W., B. McAvaney, K. Puri and R. Thuring, 1977: Global modeling of atmospheric flow by the spectral method. *Methods in Computational Physics*, No. 17, *General Circulation Models of the Atmosphere*, J. Chang, Ed., Academic Press, pp. 267–324.

Bryan, K., 1969: A numerical method for the study of the circulation of the World Ocean. *J. Comput. Phys.*, **4,** 347–376.

Daley, R., C. Girard, J. Henderson and I. Simmonds, 1976: Short-term forecasting with a multi-level spectral primitive equations model. *Atmosphere*, **14,** 98–134.

Delsol, F., K. Miyakoda and R. H. Clarke, 1971: Parameterized processes in the surface boundary layer of an atmospheric circulation model. *Quart. J. Roy. Meteor. Soc.*, **97,** 181–208.

Eliasen, E., B. Machenhauer and E. Rasmussen, 1970: On a numerical method for integration of the hydrodynamical equations with a spectral representation of the horizontal fields. Rep. No. 2, Institute for Theoretical Meteorology, Copenhagen University, Haraldsgade 6, DK 2200, Copenhagen, N Denmark, 37 pp.

Elsaesser, H. W., 1966: Expansion of hemispheric meteorological data in anti-symmetric surface spherical harmonic (Laplace) series. *J. Appl. Meteor.*, **5,** 263–276.

Fels, S. B., and M. D. Schwarzkopf, 1975: The simplified exchange approximation: A new method for radiative transfer calculation. *J. Atmos. Sci.*, **32,** 1475–1488.

Gordon, C. T., and W. Stern, 1974: Spectral modelling at GFDL. The GARP Programme on Numerical Experimentation. *Rep. Int. Symp. on Spectral Methods in Numerical Weather Prediction*, Copenhagen, WMO, Rep. No. 7, 46–80.

Hoskins, B. J., and A. J. Simmons, 1975: A multi-layer spectral model and the semi-implicit method. *Quart. J. Roy. Meteor. Soc.*, **101,** 637–655.

Keshavamurty, R. N., 1982: Response of the atmosphere to sea-surface temperature anomalies over the equatorial Pacific and the teleconnection of the Southern Oscillation. *J. Atmos. Sci.*, **39,** 1241–1259.

Lau, N. C., 1981: A diagnostic study of recurrent meteorological anomalies appearing in a 15-year simulation with a GFDL general circulation model. *Mon. Wea. Rev.*, **109,** 2287–2311.

Lorenc, A., 1981: A global three-dimensional multivariate statistical interpolation scheme. *Mon. Wea. Rev.*, **109,** 15–35.

Lubeck, O. M., T. Rosmund and R. T. Williams, 1977: Divergent initialization experiments using a spectral model. Rep. NPS-63 Wu 7799, Naval Postgraduate School, Monterey, CA, 81 pp.

Machenhauer, B., 1977: On the dynamics of gravity oscillations in a shallow water model, with applications to normal mode initialization. *Contrib. Atmos. Phys.*, **50,** 253–271.

——, and R. Daley, 1972: A baroclinic primitive equation model with a spectral representation in three dimensions. Rep. No. 4, Institute for Theoretical Meteorology, Copenhagen University, Haraldsgade 6, DK 2200 Copenhagen, N Denmark, 63 pp.

Manabe, S., and R. F. Strickler, 1964: Thermal equilibrium of the atmosphere with a convective adjustment. *J. Atmos. Sci.*, **21,** 361–385.

——, J. Smagorinsky and R. F. Strickler, 1965: Simulated climatology of a general circulation model with a hydrologic cycle. *Mon. Wea. Rev.*, **93,** 769–798.

——, 1969: Climate and the ocean circulation: I. The atmospheric circulation and the hydrology of the Earth's surface. *Mon. Wea. Rev.*, **97,** 739–774.

——, D. G. Hahn and J. L. Holloway, 1979: Climate simulation with GFDL spectral models of the atmosphere: Effect of spectral truncation. *Rep. JOC Study Conference on Climate Models: Performance, Intercomparison and Sensitivity Studies*, Vol. 1, *GARP Publ. Ser.*, No. 22, WMO, 41–94.

——, and D. G. Hahn, 1981: Simulation of atmospheric variability. *Mon. Wea. Rev.*, **109,** 2260–2286.

Mellor, G. L., and T. Yamada, 1974: A hierarchy of turbulence closure models for planetary boundary layers. *J. Atmos. Sci.*, **31,** 1791–1806.

Meleshko, V. P., and R. T. Wetherald, 1981: The effect of geographical cloud distribution on climate: A numerical experiment with an atmospheric general circulation model. *J. Geophys. Res.*, **86,** 11995–12014.

Merilees, P. E., 1968: The equations of motion in spectral form. *J. Atmos. Sci.*, **25,** 736–743.

Miyakoda, K., 1973: Cumulative results of testing a meteorological-mathematical model: The description of the model. *Proc. Roy. Irish Acad.*, **A73,** No. 9, 99–130.

——, and J. Sirutis, 1977: Comparative integrations of global models with various parameterized processes of subgrid-scale vertical transports: Description of the parameterizations. *Contrib. Atmos. Phys.*, **50,** 445–488.

——, D. Hembree and R. Strickler, 1979: Cumulative results of extended forecast experiments. II. Model performance for summer cases. *Mon. Wea. Rev.*, **107,** 395–420.

——, L. Umscheid, T. Terpstra, J. Ploshay, J. Sirutis, W. Bourke, C. T. Jobson, W. Stern and W. Davis, 1982: FGGE four-dimensional analysis system at GFDL. *Mon. Wea. Rev.*, **110** (in press).

Orszag, S. A., 1970: Transform method for the calculation of vector-coupled sums: Application to the spectral form of the vorticity equation. *J. Atmos. Sci.*, **27,** 890–895.

——, 1971: On the elimination of aliasing in finite-difference schemes by filtering high-wavenumber components. *J. Atmos. Sci.*, **28,** 1074.

Rossow, W. B., 1978: Preliminary results from a general circulation model of Venus's atmosphere (abstract). *Bull. Amer. Astron. Soc.*, **10,** 546.

——, 1979: The heat budget in a slowly rotating Venus-like model atmosphere (abstract). *Bull. Amer. Astron. Soc.*, **11,** 547.

Sela, J. G., 1980: Spectral modelling at the National Meteorological Center. *Mon. Wea. Rev.*, **108,** 1279–1292.

Simmonds, I., 1976: Data assimilation with a one-level primitive equation spectral model. *J. Atmos. Sci.*, **33,** 1155–1171.

——, 1978: The application of a multi-level spectral model to data assimilation. *J. Atmos. Sci.*, **35,** 1321–1339.

Simmons, A. J., and B. J. Hoskins, 1975: A comparison of spectral and finite difference simulations of a growing baroclinic wave. *Quart. J. Roy. Meteor. Soc.*, **101,** 551–565.

Smagorinsky, J., 1963: General circulation experiments with the primitive equations: I. The basic experiment. *Mon. Wea. Rev.*, **91,** 99–164.

——, J., S. Manabe and J. L. Holloway, Jr., 1965: Numerical results from a nine-level general circulation model of the atmosphere. *Mon. Wea. Rev.*, **93,** 727–798.

Staniforth, A. N., and R. W. Daley, 1977: A finite-element formulation for the vertical discretization of sigma-coordinate primitive equation models. *Mon. Wea. Rev.*, **105,** 1108–1118.

Umscheid, L., and P. Bannon, 1977: A comparison of three global grids used in numerical prediction models. *Mon. Wea. Rev.*, **105,** 618–635.

Wetherald, R. T., and S. Manabe, 1981: Influence of seasonal variation upon the sensitivity of a model climate. *J. Geophys. Res.*, **86,** 1194–1204.

Williams, G. P., and J. L. Holloway, Jr., 1982: Planetary circulations: Their range and unity. *Nature*, **297,** 295–297.